COGNITIVE NEUROSCIENCE

Human REM sleep recalibrates neural activity in support of memory formation

Janna D. Lendner[1,2], Niels Niethard[3], Bryce A. Mander[4], Frank J. van Schalkwijk[1], Sigrid Schuh-Hofer[5,6], Hannah Schmidt[5], Robert T. Knight[7,8], Jan Born[3,9,10], Matthew P. Walker[7,8], Jack J. Lin[11,12], Randolph F. Helfrich[1,6]*

The proposed mechanisms of sleep-dependent memory consolidation involve the overnight regulation of neural activity at both synaptic and whole-network levels. Now, there is a lack of in vivo data in humans elucidating if, and how, sleep and its varied stages balance neural activity, and if such recalibration benefits memory. We combined electrophysiology with in vivo two-photon calcium imaging in rodents as well as intracranial and scalp electroencephalography (EEG) in humans to reveal a key role for non-oscillatory brain activity during rapid eye movement (REM) sleep to mediate sleep-dependent recalibration of neural population dynamics. The extent of this REM sleep recalibration predicted the success of overnight memory consolidation, expressly the modulation of hippocampal—neocortical activity, favoring remembering rather than forgetting. The findings describe a non-oscillatory mechanism how human REM sleep modulates neural population activity to enhance long-term memory.

INTRODUCTION

Contemporary theories of sleep function proposed that the overnight regulation of excitability constitutes a physiologic mechanism underlying neural network plasticity, facilitating memory consolidation during sleep (*1*–*4*). In vivo animal studies have revealed that wakefulness and learning lead to a progressive excitability increase (*2*, *5*, *6*). It has been proposed that sleep renormalizes excitability and eliminates synapses [termed "down-scaling" or "pruning" (*5*, *7*–*9*)]. Thus, sleep may restore the optimal neurobiological milieu for learning and strengthen memory representations (*2*, *10*). That such mechanisms take place in the human brain remains largely speculative. Specifically, the concept of a cellular or network-level process in the human brain, involving the recalibration of neural activity during sleep, has remained untested. In addition, the potential benefits of such a mechanism for memory retention remain unexplored. One reason for this paucity of knowledge, relative to animal models (*11*, *12*), is the lack of electrophysiological markers that link cellular properties, such as excitability, to whole-brain network dynamics, amenable to electroencephalography (EEG).

To date, the majority of the evidence for sleep-dependent cellular and network homeostasis suggests that slow oscillations (SOs; <1.25 Hz) during NREM (nonrapid eye movement) sleep may mediate the regulation of neural excitability (*2*, *10*). Considerably less evidence exists regarding a similar role for REM sleep, with limited data in rodents suggesting that theta activity (4 to 10 Hz) may offer similar functional benefits (*8*, *13*). Theta oscillations during REM sleep are prominent only in rodents, whereas human REM sleep is characterized by desynchronized EEG activity without prominent oscillations (*14*). This leads to the currently unexamined possibility that traditional oscillation-based analyses might insufficiently capture functionally measurable processes of overnight recalibration of neural activity in human REM sleep.

Several computational models indicate that desynchronized, non-oscillatory brain activity (also termed aperiodic activity for the lack of a defining temporal scale) correlates with population excitation-to-inhibition balance [as defined by the activity ratio between excitatory and inhibitory neurons; E-I ratio; (*15*, *16*)]; thus, constituting a promising proxy EEG marker of neural excitability (*15*–*17*). Aperiodic activity is typically quantified by the spectral slope x of the $1/f^x$ decay function of the electrophysiological power spectrum [or power spectral density (PSD) function] in log-log space. Thus, increased aperiodic neural activity encompasses a flattening of the PSD and an increase in the spectral slope, while decreased aperiodic activity is reflected in a steepening of the PSD and a decreased slope. While direct experimental evidence for this hypothesis remains scarce, aperiodic activity provides a possible theoretical framework to link the sleep-dependent regulation of neural activity in humans to overnight memory consolidation. Here, we assessed neural excitability at the population level using two different approaches. First, we examined calcium activity of pyramidal cells and the ratio of activity between excitatory pyramidal cells and interneurons, using two-photon imaging. While calcium activity is an indicator of calcium entry in the cells upon neural firing (*18*), calcium activity does not directly quantify firing, excitation, or inhibition; hence, we approximated excitability at the

[1]Hertie Institute for Clinical Brain Research, Center for Neurology, University Medical Center Tübingen, Hoppe-Seyler-Str 3, 72076 Tübingen, Germany. [2]Department of Anesthesiology and Intensive Care Medicine, University Medical Center Tübingen, Hoppe-Seyler-Str 3, 72076 Tübingen, Germany. [3]Institute of Medical Psychology and Behavioral Neurobiology, University of Tübingen, Tübingen 72076, Germany. [4]Department of Psychiatry and Human Behavior, UC Irvine, 101 The City Dr, Orange, CA 92868, USA. [5]Department of Neurophysiology, University Medical Center Mannheim, Ludolf-Krehl-Str. 13-17, 68167 Mannheim, Germany. [6]Department of Neurology and Epileptology, University Medical Center Tübingen, Hoppe-Seyler-Str 3, 72076 Tübingen, Germany. [7]Helen Wills Neuroscience Institute, UC Berkeley, 130 Barker Hall, CA 94720, USA. [8]Department of Psychology, UC Berkeley, 2121 Berkeley Way, CA 94720, USA. [9]Center for Integrative Neuroscience, University of Tübingen, Tübingen 72076, Germany. [10]German Center for Diabetes Research (DZD), Institute for Diabetes Research and Metabolic Diseases of the Helmholtz Center Munich at the University of Tübingen (IDM), Tübingen 72076, Germany. [11]Department of Neurology, UC Davis, 3160 Folsom Blvd., Sacramento, CA 95816, USA. [12]Center for Mind and Brain, UC Davis, 267 Cousteau Pl, Davis, CA 95618, USA.
*Corresponding author. Email: randolph.helfrich@gmail.com

population level by means of pyramidal cell activity and their activity ratio with interneurons. Second, we used the EEG spectral slope to quantify aperiodic activity. Subsequently, we directly tested the relationship between these meso- and macroscale surrogate markers of neural excitability.

Since theoretical accounts suggested that synaptic downscaling could benefit sleep-dependent memory consolidation (*1*, *2*, *19*), the key hypothesis was that aperiodic activity, quantified by the spectral slope as a EEG-based proxy of neural excitability (*20*), increases during the day and decreases after sleep; thus, constituting a down-regulation of a putative EEG-based metric of population excitability. Conversely, sleep loss should abate a sleep-dependent regulation. We hypothesized that human REM sleep, which previously has been shown to exhibit the strongest spectral slope reduction (*14*, *21*, *22*), might mediate the overnight modulation of aperiodic activity. If down-regulation of aperiodic activity is functionally relevant, then the degree of its modulation should predict individual's memory retention.

RESULTS

Two definitions of population excitability and E-I (excitatory-inhibitory) ratio are used, depending on the spatial scale. At the cellular/mesoscale level in rodent experiments, we evaluated the activity of pyramidal neurons, which we referred to as "excitability," along with their ratio of activity with interneurons, termed "E-I ratio"; thereby approximating the E-I definition used in computational models (*15*, *16*, *20*). Subsequently, we examined whether the observed neuronal activity was reflected in the dynamics of aperiodic brain activity recorded from the rodent scalp EEG, quantified by the spectral slope. At the network level in human recordings, we then investigated whether the dynamics of aperiodic brain activity could serve as a surrogate marker of overnight excitability recalibration.

To test the relationship between population dynamics and aperiodic activity, we first analyzed a previously published dataset that included simultaneous cortical in vivo two-photon calcium imaging and scalp electrophysiology during rodent sleep (*21*). We tested whether aperiodic EEG activity captures mesoscale neural excitability (as defined by pyramidal cell calcium activity) and the activity ratio between excitatory pyramidal cells and inhibitory interneurons (E-I ratio) of the underlying neural population (study 1; N = 8 animals, 1486 cells). We further included a control study with simultaneous hippocampal and scalp recordings in sleeping rodents to assess regional specificity (study S1; N = 5 animals; fig. S1).

Next, we acquired both invasive and noninvasive electrophysiological recordings in humans to test whether an overnight regulation of aperiodic activity supported memory consolidation, by combining an episodic memory task (*23*, *24*) with resting state scalp EEG recordings before, during, and after habitual sleep (study 2; N = 40 participants), as well as after sleep deprivation (study 3; N = 12 participants). Furthermore, we examined aperiodic activity in overnight sleep recordings in simultaneous scalp and intracranial EEG recordings (study 4; N = 15 participants; 498 bipolar contacts) in patients with pharmacoresistant epilepsy that underwent invasive monitoring.

Aperiodic activity reflects neural population activity in rodents

Computational models posit aperiodic activity captures population activity of excitatory and inhibitory interneurons (*15*, *20*), but these assumptions lack empirical evidence. To determine whether aperiodic EEG activity captures population dynamics during sleep, we combined scalp electrophysiology with in vivo two-photon calcium imaging in mouse cortex (Fig. 1A; 14 recordings in eight animals) of pyramidal cells (N = 1242) and interneurons [parvalbumin-positive (PV^+) interneurons, N = 132 cells; and somatostatin-positive (SOM^+) interneurons, N = 112 cells]. Excitability was defined as the overall calcium activity in pyramidal cells (quantified as active frames, see below). Cell type–specific activity was strongly modulated by different sleep stages. Overall pyramidal cell calcium activity was lower during sleep than wakefulness {Fig. 1B; Pyr: P = 0.0150, $t_{40} = -2.51$, 95% confidence interval (CI_{95}) = $[-5 \times 10^{-3}\ -6 \times 10^{-4}]$; PV^+: P = 0.0330, t_{19} = 2.30, $CI_{95} = [8 \times 10^{-4}\ 1.9 \times 10^{-2}]$; SOM^+: $P < 0.0001$, $t_{19} = -7.93$, $CI_{95} = [-10^{-2}\ -7 \times 10^{-3}]$; linear mixed effect (LME) models}. Layer 2/3 pyramidal cell activity was lowest during REM sleep. A similar pattern was evident for SOM^+ interneurons, while PV^+ interneurons exhibited an activity increase during REM sleep. At the mesoscale, these findings may reflect an excitability decrease during REM sleep (Fig. 1B).

Spectral parametrization of simultaneously recorded frontal EEG activity revealed a sleep-stage–specific modulation of aperiodic background activity (Fig. 1C and fig. S1; $P < 0.0001$, $F_{1.74,12.15}$ = 23.46; repeated measures analysis of variance (RM-ANOVA), averaged across sessions; wake: −2.84 ± 0.05; NREM: −3.35 ± 0.04; REM: −2.97 ± 0.10; mean ± SEM), which largely captured hippocampal contributions (fig. S1). We extracted calcium transients (active frames) from the continuous fluorescence signal (Fig. 1D) to determine whether the cell-specific calcium activity predicted aperiodic EEG activity. Putative excitatory (pyramidal) cell activity and inhibitory (interneuron) activity were strongly correlated (Spearman rho = 0.76, $P < 0.0001$). Moreover, their relationship was systematically biased toward interneuron activity in states of high overall activity (Fig. 1, E and F); thus, confirming and extending previous electrophysiological findings (*25*, *26*). Specifically, an increase in pyramidal cell calcium activity was counterbalanced by a net increase in inhibitory interneuron activity (Fig. 1E, regression slope 1.22 ± 0.05, mean ± SEM; P = 0.0041, t_7 = 4.18, d = 1.48; two-tailed t test against 1). In addition, this same relationship was also evident when overall activity was contrasted against the population E-I ratio (defined as the difference between the average pyramidal cell and interneuron activity; balanced at 0, bounded at ±1; Fig. 1F, regression slope −0.35 ± 0.05; mean ± SEM; $P < 0.0001$, $t_7 = -22.16$, d = 2.10; two-tailed t test against 0).

To directly test the relationship of population dynamics and aperiodic EEG activity (illustrated in Fig. 1G), we first discretized the calcium activity into four quartiles relative to either the current excitatory pyramidal cell activity (Fig. 1H) or the momentary balance between pyramidal cell and interneuron activities (Fig. 1I) and assessed EEG aperiodic activity as a function of the quartiles (Q; ranging from 1 to 4 = low to high).

In line with the model predictions (*15*, *16*), the spectral slope increased (flattening of the PSD) as a function of pyramidal cell activity (Fig. 1H, right; $P < 0.0001$; t_{54} = 5.67, CI_{95} = [0.12 0.25], LME; slope Q1 = −2.94 ± 0.04; Q4 = −2.39 ± 0.14; mean ± SEM). Moreover, the spectral slope decreased (steepened) when the E-I ratio

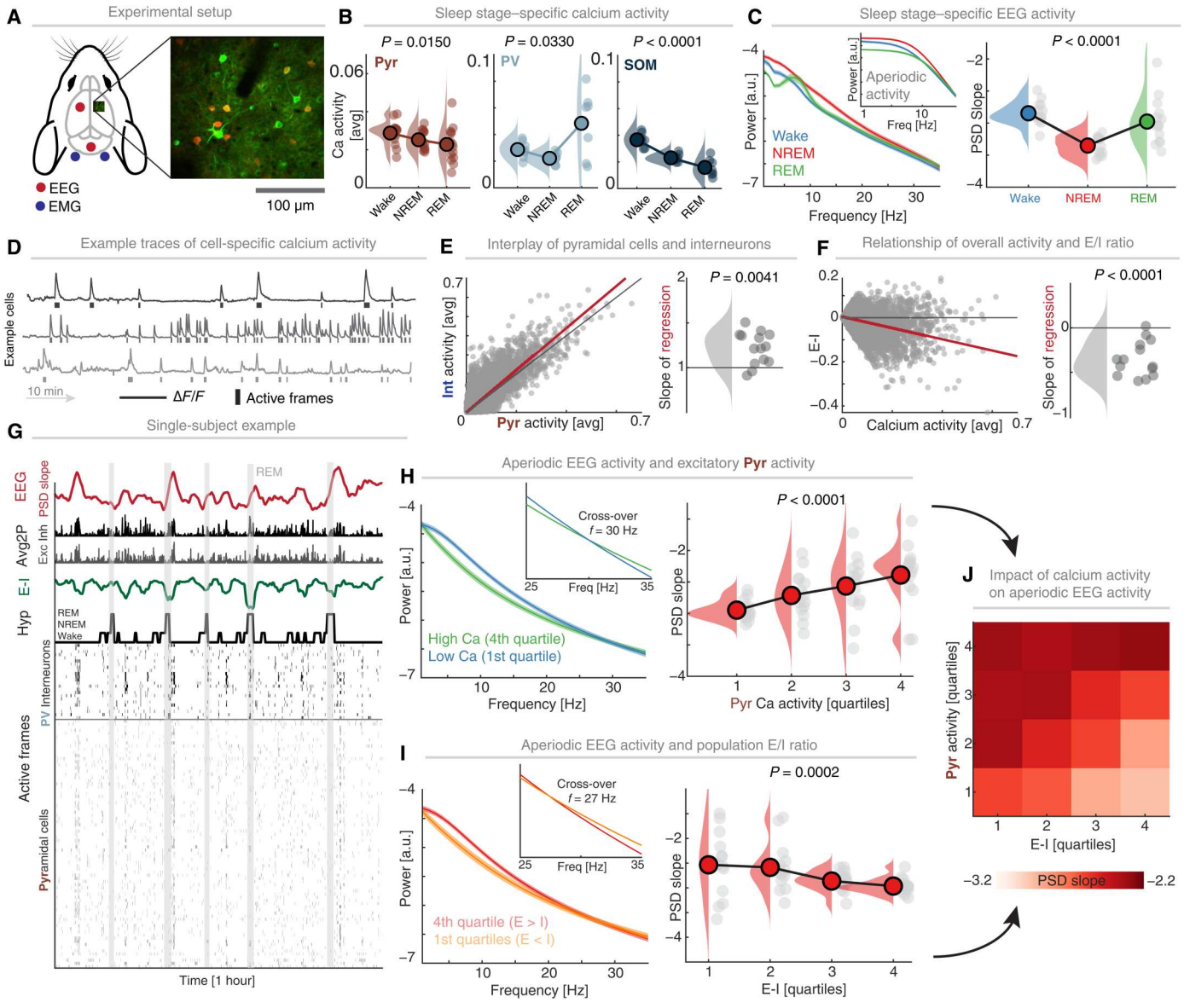

Fig. 1. Aperiodic activity tracks population dynamics in vivo. (**A**) Experimental setup [schematic; (*72*)]. Representative in vivo two-photon calcium image of pan-neuronally expressed GCaMP6f (green) and cre-dependent tdTomato (red) in layer 2/3. (**B**) Calcium activity varied between sleep stages. Left, pyramidal cells (Pyr); center, parvalbumin-positive (PV^+) interneurons; right, somatostatin interneurons (SOM^+). (**C**) Left: EEG power spectra (inset: aperiodic component (log-log); frontal electrode). Right: PSD slope (cf. fig. S1). (**D**) Fluorescence traces from exemplary pyramidal cells. Tick marks highlight active frames. (**E**) Left: Relationship of excitatory (Pyr) and inhibitory (PV^+/SOM^+) activity. The black line indicates the diagonal (balanced regime). Linear regression (red) highlights a biased relationship with a net increase of inhibitory drive during high excitation. Right: Statistical quantification. (**F**) Left: Relationship of calcium activity and excitation to inhibition ratio (E-I; balanced at 0, bounded at ±1; red line: linear regression; black line: balanced regime). Right: Statistical quantification. (**G**) PV^+ mouse example (~1 hour) demonstrating the relationship (top-to-bottom) of the PSD slope (red), average activity (black: PV^+; grey: Pyr), E-I (green), and the hypnogram. The raster highlights all interneurons (black, PV^+) and pyramidal cells (grey). Note the relationship of the PSD slope and E-I (pronounced during REM sleep; gray shaded). (**H**) EEG activity relative to active frames quartiles (low to high). Left: PSDs, first and fourth quartiles (cross-over at 30 Hz; inset). Right: Spectral slope as a function of Pyr activity quartiles. (**I**) EEG activity relative to E-I quartiles (low to high). Left: PSDs, first and fourth quartiles (cross-over at 27 Hz; inset). Right: Spectral slope as a function of E-I quartiles. (**J**) Composite slope representation as a function of pyramidal cell activity and E-I. A flattening of the PSD slope (dark red) is evident during high Pyr activity (top row). Aperiodic activity is mainly correlated with E-I during low excitatory activity (bottom row). a.u., arbitrary units.

shifted toward increased pyramidal cell activity (Fig. 1I, right; P = 0.0002, t_{54} = −3.96, CI_{95} = [−0.24 −0.08], LME; slope Q1 = −2.53 ± 0.17; Q4 = −2.96 ± 0.04; mean ± SEM). While the spectral slope also covaried with the activity (putative E-I) ratio between pyramidal cells and interneurons (cf. Fig. 1I), this relationship was pronounced when pyramidal cell activity was low (Fig. 1J, bottom row, Q1 versus Q4: Cohen's d = 0.88) as compared to when activity was high (top row Q1 versus Q4: d = 0.04). The observed pattern remained highly comparable when only a single state (e.g., wakefulness) was considered: The spectral slope increased (flattened) when pyramidal cell calcium activity was high (P < 0.0001; t_{54} = 7.35, CI_{95} = [0.15 0.27], LME; slope Q1 = −2.86 ± 0.04; Q4 = −2.22 ± 0.13; mean ± SEM). The spectral slope decreased (steepened) when pyramidal cell activity was higher than interneuron activity (E-I quartiles; P < 0.0001, t_{54} = −6.30, CI_{95} = [−0.26 −0.13], LME; slope Q1 = −2.32 ± 0.14; Q4 = −2.86 ± 0.05; mean ± SEM). Again, the spectral slope covaried with the population E-I ratio, and this relationship was pronounced when pyramidal cell activity was low (Q1 versus Q4: Cohen's d = 1.62) as compared to when activity was high (top row Q1 versus Q4: d = −0.11).

This observation is the direct result of the mutual dependence and recurrent interactions between excitatory pyramidal cells and inhibitory interneurons in neural circuits (cf. Fig. 1, E and F), while the model assumed a linear independent summation (*15*). In addition to the robust relationship across the entire night, aperiodic activity also tracked mesoscale properties on the time scale of single REM sleep epochs (fig. S2). Collectively, this set of findings indicates that the EEG aperiodic activity as quantified by the spectral slope indexes excitability dynamics at the mesoscale using calcium imaging (Fig. 1J).

Aperiodic activity is modulated during sleep in humans

We next sought to test whether a modulation of aperiodic activity similarly occurred during human sleep. Here, we used resting state scalp EEG (19-channel, 10–20 layout) recordings in three cognitive states (cognitive engagement during backward counting, rest eyes closed, and fixation) before and after a night of habitual sleep (N = 40; fig. S3). Spectral analysis revealed a broadband power decrease after sleep in all frequencies above 11 Hz and across the majority of EEG sensors (Fig. 2A; averaged across all conditions, cluster test; P = 0.0020, d = 0.86). This broadband modulation was driven by changes of non-oscillatory aperiodic brain activity (fig. S3, A and B). The spectral slope was more negative after habitual sleep, with the peak effect over frontal EEG sensors (inset Fig. 2A; cluster test; P = 0.0180, d = 0.32; electrode Fz: PM: −2.76 ± 0.03, AM: −3.04 ± 0.03; mean ± SEM). These findings demonstrate that aperiodic activity undergoes an overnight modulation.

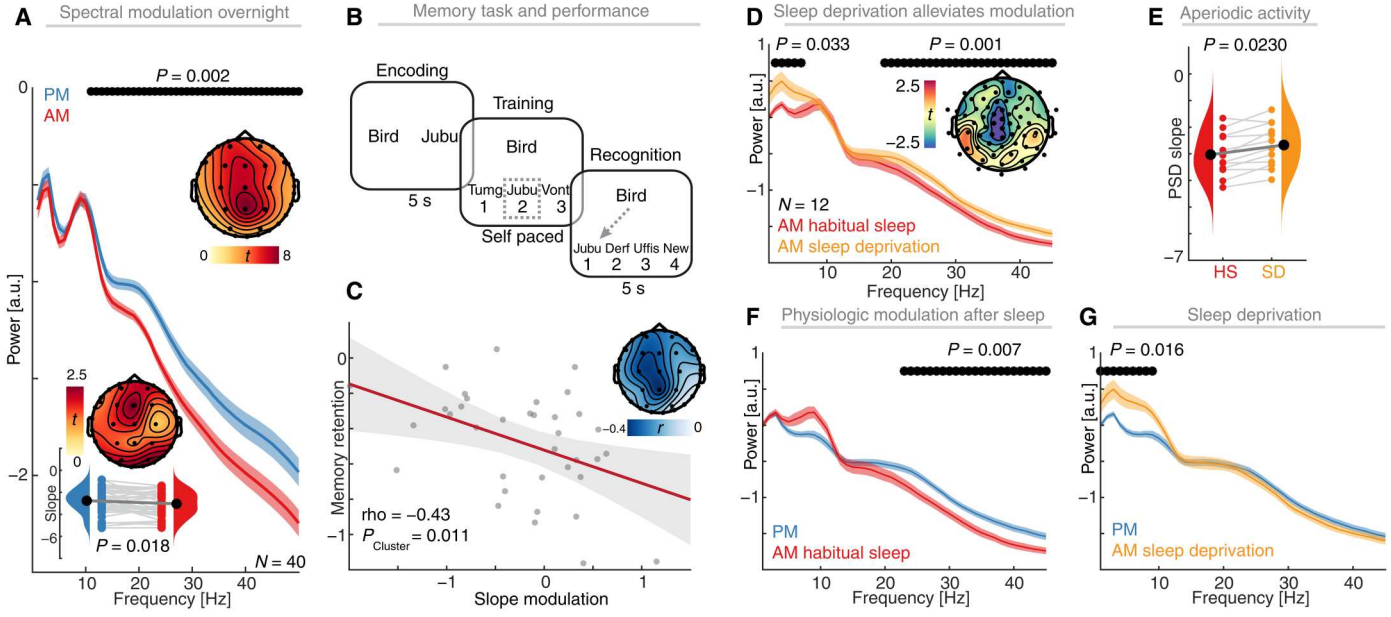

Fig. 2. Overnight modulation of aperiodic activity predicts memory retention and is attenuated by sleep deprivation. (**A**) Grand average EEG PSDs (semi-log) before (blue, PM) and after (red, AM) habitual sleep (N = 40; averaged across all cluster electrodes and three conditions: cognitive engagement, eyes closed, and central fixation; see also fig. S3) indicate a broadband power decrease (11 to 50 Hz) after sleep (inset top right; colormap indicates t values; large black dots indicate significant electrodes in the cluster). Inset lower left: The spectral slope decreased over frontal sensors (visualized at Fz; colormap reflects t-values). (**B**) Episodic word pair task. Participants learned 120 word-nonsense word associations. After encoding (left), participants were trained to criterion (center) before sleep and then performed recognition test before and after sleep (right). (**C**) Cluster-corrected correlation analysis revealed a significant association between slope modulation and memory retention: Participants who showed a stronger slope decrease from PM to AM exhibited better memory retention (slope averaged across all significant electrodes in cluster; colormap indicates correlation coefficients). (**D**) Eyes open resting state recordings in the AM (red, habitual sleep; orange, sleep deprivation) reveal a broadband power increase after sleep deprivation (N = 12; within-subject design; cluster test: cluster 2 to 6Hz, P = 0.04; cluster 19 to 47 Hz, P = 0.0040; visualized at Cz) over central sensors (inset; large black dots indicate significant cluster; colormap reflects t value). (**E**) This broadband power modulation was the result of an increase of the spectral slope after sleep deprivation (P = 0.023; averaged over all cluster channels). (**F**) Comparison to presleep eyes open recordings (PM, blue) replicates the broadband down-regulation [cf. (A) and (B)], while (**G**) sleep deprivation attenuates this effect (common electrode Cz in studies 2 and 3) and increased low-frequency activity.

Overnight modulation of aperiodic activity predicts successful memory retention in humans

Having established an overnight modulation of aperiodic activity across sleep in humans, we next investigated whether this modulation was functional (rather than epiphenomenal), specifically examining whether such modulation predicted overnight memory retention. Participants performed a validated sleep-dependent episodic memory test [Fig. 2B; 36 subjects completed behavioral testing; (*23*)]. After encoding, participants were trained to criterion before initial recognition testing in the evening (PM) (*23*, *24*). After 8 hours of sleep starting at their habitual bedtime, they performed the second recognition test the next morning (AM). Participants who exhibited a stronger modulation of aperiodic activity (decrease of the spectral slope; slope modulation = AM minus PM) demonstrated better memory retention (Fig. 2C; cluster test; $P = 0.0011$; mean rho = −0.36; fig. S3D). This effect was not confounded by electromyogram (EMG) activity or age (fig. S3, B to D; Spearman partial correlation at Fz: EMG: rho = −0.45, $P = 0.0069$; age: rho = −0.46, $P = 0.0050$) and was most pronounced for the frequency range above 20 Hz (fig. S3, E to G). Collectively, this set of findings demonstrated that down-regulation of aperiodic brain activity across the night predicts the overnight consolidation of episodic memory that determines the next-day retention.

Sleep deprivation attenuates overnight regulation of aperiodic activity in humans

Having characterized the spatiotemporal extent of the overnight regulation, we next assessed the causal role for sleep in the modulation of aperiodic activity across the night in an independent cohort that was sleep deprived ($N = 12$; eyes open, central fixation; 64 channel, equidistant layout, centered on electrode Cz). Sleep deprivation resulted in a broadband power increase over central sensors compared to posthabitual sleep (inset Fig. 2D; cluster test; $P = 0.0030$, $d = 0.81$), evident as a flattening of the spectral slope (Fig. 2E; $P = 0.023$, $d = 0.90$; cluster test; posthabitual sleep: −3.03 ± 0.23; sleep deprivation: −2.71 ± 0.23). Statistical comparison to presleep resting states (PM; cf. Fig. 1A; between-subject design) revealed a broadband power decrease after sleep, directly replicating the results from study 2 (Fig. 2F; cluster test; $P = 0.0070$, $d = 0.81$; cluster-corrected unpaired *t* tests). Sleep deprivation attenuated the modulation of aperiodic activity (Fig. 2G; $d = 0.27$ instead of $d = 0.81$; cf. Fig. 2F) and led to an increase of low frequency activity [cluster test; 1 to 9 Hz; $P = 0.0160$, $d = 1.23$, a finding in line with observations of enhanced slow waves after prolonged wakefulness (*27*)]. Together, these findings establish that sleep deprivation attenuates the down-regulation of aperiodic brain activity.

REM sleep predicts modulation of aperiodic activity

Next, we tested the hypothesis that REM sleep mediates the observed down-regulation of aperiodic activity in humans. Previously, REM sleep theta oscillations have been associated with reorganizing neural excitability (as defined by the overall firing rate) in rodents (*8*). However, theta oscillations are less prevalent during human REM sleep (figs. S1 and S4, A and B), which is characterized by desynchronized EEG activity. Therefore, we tested whether a non-oscillatory mechanism during REM predicted the modulation from one NREM epoch to the next one. Consistent with previous findings in humans [(*14*, *22*); cf. fig. S1], the spectral slope was more negative during REM sleep (Fig. 3A; one-way ANOVA: $F_{2.9,75.3} = 61.78$, $P < 0.0001$; wake: −3.18 ± 0.15; NREM: −3.41 ± 0.07; REM: −4.41 ± 0.15; electrode Fz) compared to NREM (post hoc paired *t* test: $t_{39} = 8.20$, $P < 0.0001$, $d = 1.30$) and wakefulness ($t_{39} = 11.58$, $P < 0.0001$, $d = 1.83$). This observation confirms that REM sleep is associated with the most profound reduction of aperiodic activity during human sleep (*14*), particularly over frontal EEG sensors. Note that this observation reflects a dissociation between human (REM slope < NREM slope) and rodent REM sleep (NREM slope < REM slope). However, this apparent discrepancy mainly reflects a technical issue given the strong hippocampal contribution to the frontal scalp EEG in rodents (fig. S1), while hippocampal dynamics were highly comparable across both species.

When contrasting the first and last NREM segments of the night, a broadband spectral power modulation was evident (Fig. 3B; $P < 0.001$, $d = 0.80$; cluster-corrected permutation test based on paired *t* tests) with a similar spatial extent as the effect across the night (cf. Fig. 2A and fig. S4C) and encompassed the canonical delta band (<4 Hz). The broadband modulation was the result of a steepening of the spectral slope ($t_{39} = 2.40$; $P = 0.0214$, $d = 0.38$; paired two-tailed *t* test). When directly contrasting the first and last REM episodes of the night, modulations were band-limited (Fig. 3C; cluster test; cluster 1 to 23 Hz, $P = 0.0090$, $d = 0.55$; cluster 28 to 40 Hz, $P = 0.0380$, $d = 0.39$) and were not driven by a change in aperiodic activity ($t_{39} = -0.65$, $P = 0.2574$, $d = -0.10$; paired two-tailed *t* test).

To determine whether REM sleep mediates the modulation of aperiodic activity in subsequent NREM epochs, time-normalized triplets of NREM-REM-NREM sleep were extracted [Fig. 3D and fig. S5 for a complementary time normalization strategy analogous to (*8*)]. State-specific oscillatory patterns (Fig. 3D, middle) were only apparent after subtraction of aperiodic activity from broadband power spectra (Fig. 3D, top). Aperiodic activity, quantified as the spectral activity slope, was strongly modulated over the course of the triplet (Fig. 3D, bottom, cluster test; $P = 0.001$, $d = 0.97$).

Consistent with a modulatory influence of REM sleep on NREM, a more negative spectral slope (i.e., a stronger down-regulation of aperiodic activity) was observed in NREM epochs after a REM episode compared to before (Fig. 3E; paired two-tailed *t* test; $t_{39} = 4.04$, $P = 0.0002$, $d = 0.64$). This effect was most pronounced in the first third of the respective NREM epoch (fig. S5G). On an individual level, a more negative spectral slope in REM sleep predicted a stronger modulation across the triplet (Fig. 3F; cluster test; $P = 0.001$, mean rho = 0.44; peak correlation at Fz rho = 0.65). This relationship between REM slope and NREM slope modulation remained unchanged after accounting for theta power (partial correlation: rho = 0.59, $P < 0.0001$) and was also apparent when the REM slope was correlated against the individual difference between first and last NREM segments of the night (Fig. 3G; cluster test; $P = 0.0470$, mean rho = 0.36; cf. Fig. 3B). Moreover, this effect was not confounded by SO power (fig. S4D; Spearman partial correlation; rho = 0.37, $P = 0.0189$) or REM theta power (partial correlation; rho = 0.34, $P = 0.0349$).

We also tested whether slow wave activity (duration, amplitude, and quantity) predicted the down-regulation of aperiodic activity across the night but did not find consistent evidence for this (fig. S6). The overnight NREM slope modulation reliably predicted individual memory performance (Fig. 3H; cluster test; $P = 0.049$, mean rho = −0.34) and became even more robust after accounting

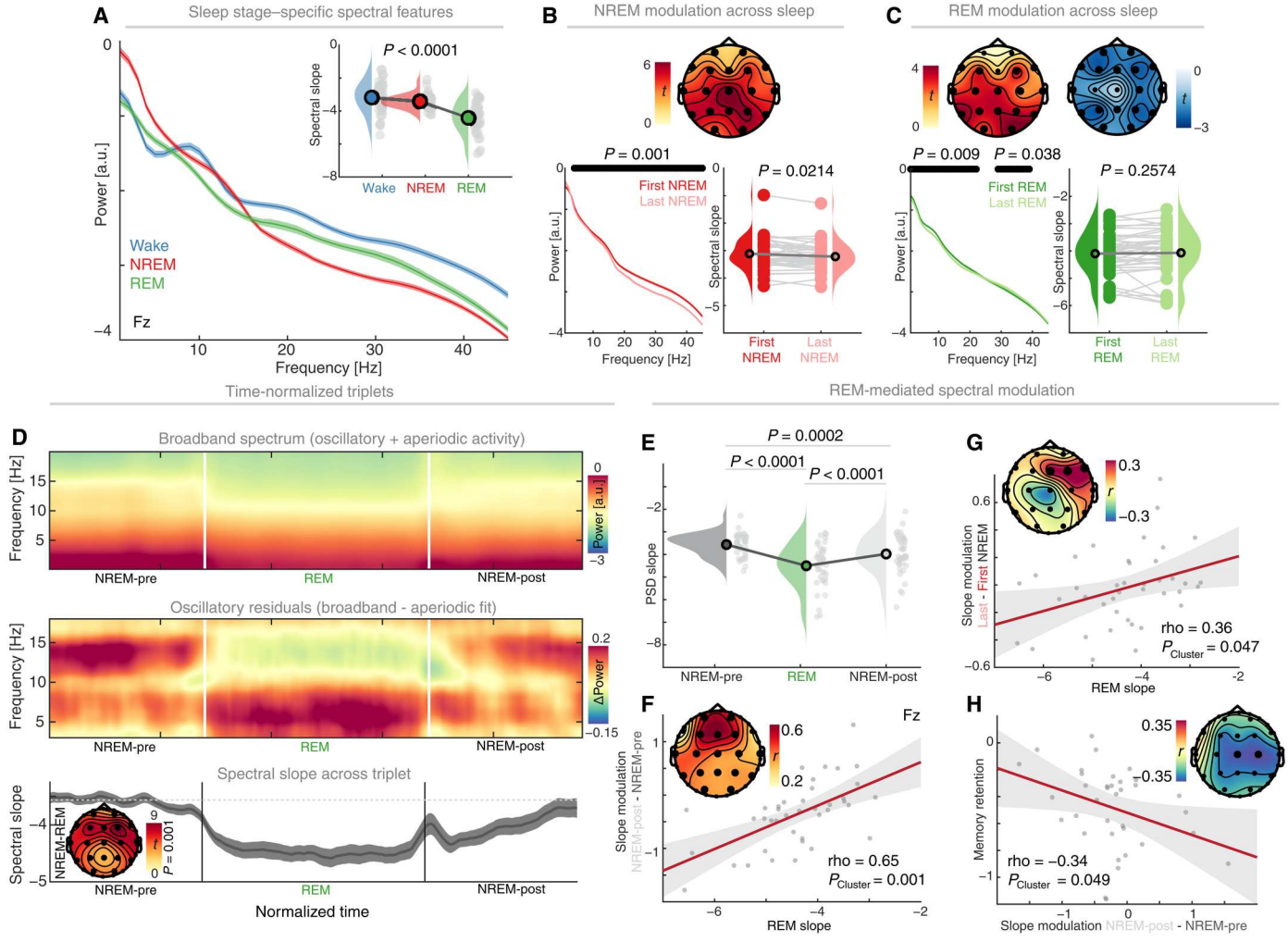

Fig. 3. Aperiodic activity during REM sleep mediates overnight broadband spectral modulation and memory retention. (**A**) Grand average power spectra for different sleep stages (semi-log; Fz). Inset: State-specific dissociation of the spectral slope. (**B**) Spectral modulation across NREM sleep demonstrates a brain-wide (top), broadband power reduction (bottom left), which was captured by a decrease of the spectral slope (bottom right). Summary statistics averaged across all electrodes in the cluster (black dots; colormap reflects *t* values). (**C**) Spectral modulation across REM sleep shows a widespread (top), frequency-specific (bottom left) effect, which left the spectral slope unchanged [same conventions as in (B)]. (**D**) Top: Time-normalized triplet (cf. fig. S5) of adjacent NREM-REM-NREM segments (Cz, young adults to attenuate the spindle slowing-related spectral smearing). Middle: Spectral residuals after subtraction of aperiodic activity revealed state-specific oscillatory signatures (NREM: spindles ~14 Hz; REM: theta at ~6 Hz). Bottom: Spectral slope over time across all subjects (at cluster peak; electrodes F3, Fz, and F4). Note a decrement during REM sleep followed by a net decrease in the subsequent NREM segment. Inset: Topographical depiction of slope differences between NREM and REM sleep. (**E**) Spectral slopes across the triplets (averaged over F3, Fz, and F4). (**F**) The spectral slope during REM sleep predicted the difference from NREM-pre to NREM-post (topography depicts spatial extent; large black dots indicate the significant cluster, colormap reflects correlation coefficients), i.e., the steeper the slope during REM, the larger the down-modulation between the adjacent NREM segments. (**G**) A similar pattern was observed over frontal sensors, when the average REM slope was correlated against the difference between first and last NREM segment of the night [cf. (B); same conventions as in (F)]. (**H**) A large REM sleep–dependent down-regulation of the slope across NREM sleep predicted better memory performance [same conventions as in (F); cf. Fig. 1D).

for theta power (partial correlation; rho = −0.49, $P = 0.0025$). Collectively, these observations indicate that REM, in concert with NREM sleep, predicts a sleep-dependent reduction of aperiodic activity that predicted memory retention.

Distinct aperiodic activity regimes govern REM sleep in MTL and PFC in humans

Regional population activity was assessed in intracranial recordings ($N = 15$ participants, 498 bipolar contacts) in two key nodes of the human memory network, the prefrontal cortex (PFC) and the medial temporal lobe (MTL). Contemporary theoretical frameworks posit that long-term memory consolidation is associated with human PFC plasticity (*1*, *28*). Hence, we tested whether the modulation of aperiodic activity differentially affects PFC and MTL. Analogous to previous work (*8*, *9*), a set of parameters was obtained in the MTL and PFC (Fig. 4A).

Across the night (comparison of the first and last third of the entire aggregated NREM sleep; Fig. 4B), the count of SOs (one-way RM-ANOVA across all thirds; $F_{1.6,22.2} = 8.01$, $P = 0.0041$, $d = 0.90$), spindles ($F_{1.7,24.4} = 8.76$, $P = 0.0020$, $d = 1.10$), and the slope

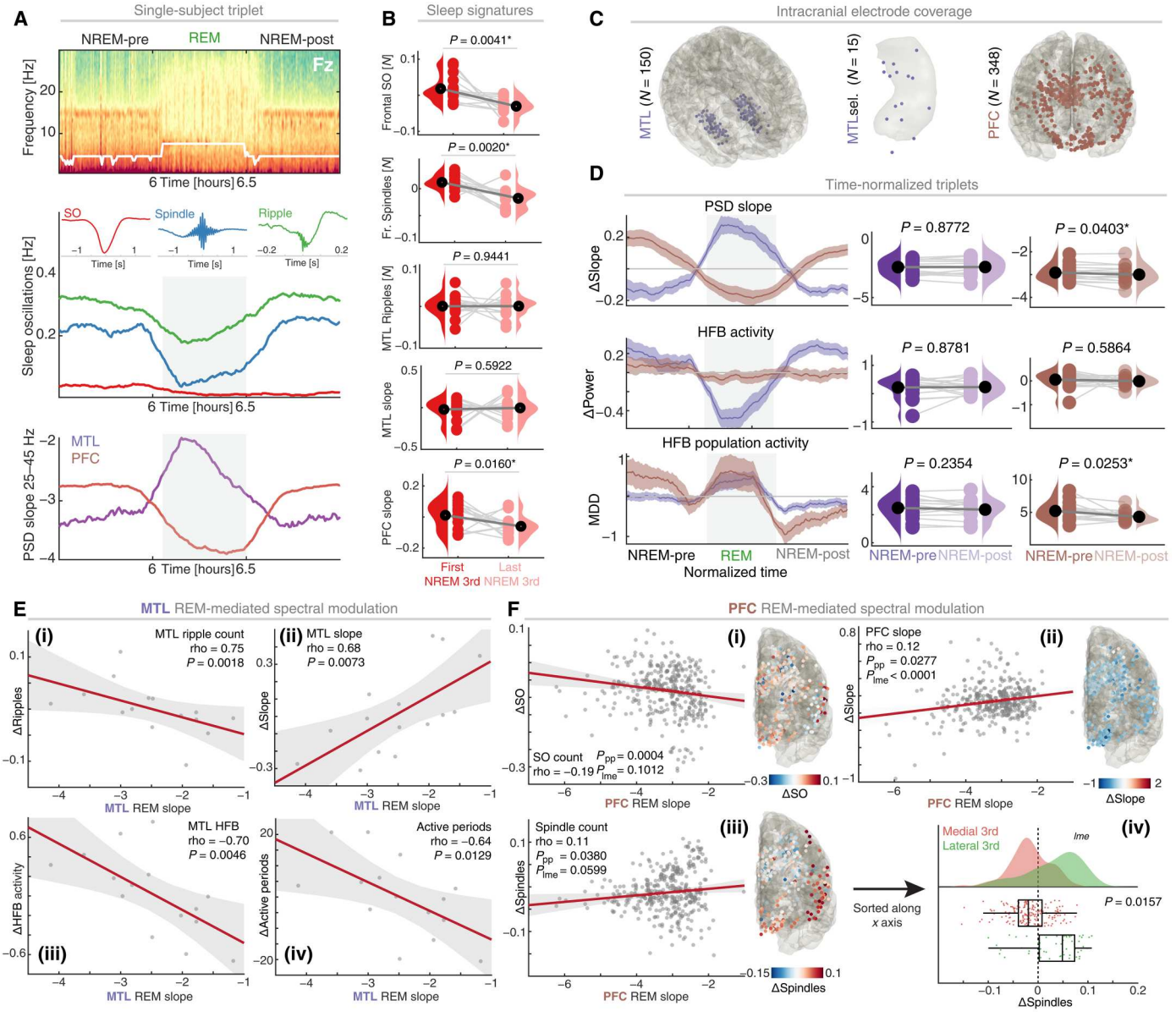

Fig. 4. Aperiodic activity changes overnight and functionally dissociates MTL and PFC. (**A**) Top: Single-subject triplet (Fz). Middle: Waveform shapes of frontal SOs (red), spindles (blue), MTL ripples (green), and their rate modulation across the triplet. Bottom: Average spectral slopes (MTL and PFC) across the triplet reveal a dissociation, with a flattening of the spectral slope in MTL during REM and a steepening in PFC. (**B**) Different sleep signatures. Δ indicates difference of last NREM minus first NREM third of the night, highlighting significant reductions in SO and spindle counts as well as PFC spectral slope. (**C**) Simultaneous electrode coverage ($N = 15$) in MTL and PFC. One MTL channel per participant was selected (the lowest number of epileptic discharges outside of seizure onset zone). (**D**) Row 1: Spectral slope time-resolved across the NREM-REM-NREM triplets (Δslope indexes modulation relative to the mean). We observed a reduction (steepening) of the spectral slope in NREM-post as compared to NREM-pre in PFC but not MTL. Row 2: Average high-frequency power (HFB; 120 to 200 Hz) shows no modulation in PFC and only little modulation across the triplet in MTL. Row 3: Population activity (multidimensional distance; MDD) highlights a dispersion of population dynamics during REM, with a net decrease in PFC. (**E**) MTL: Rank correlations between REM slope and different sleep signatures (Δ indicates last third to first). A more negative REM slope in the MTL was associated with an increase in (i) MTL ripples, (ii) a MTL slope steepening, (iii) increased HFB, and (iv) more active periods. (**F**) The same analysis for the PFC showed a REM-mediated modulation of (i) SOs, (ii) PFC slope, and (iii) spindles [*P* values are reported from the Spearman correlation (pseudo-population (pp) and an LME model]. In addition, a significant relationship between REM slope and regionally specific spindle expression was evident (iv).

($F_{1.8,25.6}$, $P = 0.0160$, $d = 0.57$; all other markers $P > 0.5$) showed statistically significant decreases in the PFC. Subsequently, NREM-REM-NREM triplets for all subjects were extracted separately for MTL and PFC (Fig. 4C and fig. S7). A state- and region-specific modulation of the spectral slope was observed (Fig. 4D) with a prominent functional dissociation between the MTL and PFC [Fig. 4D; two-way RM-ANOVA; region of interest (ROI): $F_{1,14} = 9.38$, $P = 0.0084$; state: $F_{1.2,17.1} = 0.64$, $P = 0.4672$; interaction: $F_{1.2,17.7} = 21.95$, $P = 0.0001$]. This analysis revealed a steepening of the PFC power spectrum during REM sleep (cf. Fig. 3D; paired two-tailed t test; $t_{14} = 3.44$, $P = 0.0039$, $d = 0.89$) as well as a net decrease in aperiodic activity in NREM sleep after a REM episode (replication of Fig. 3E; $t_{14} = 2.26$, $P = 0.0403$, $d = 0.58$). Critically, the pattern was reversed in the MTL (increase of the spectral slope during REM; $t_{14} = -4.68$, $P = 0.0004$, $d = 1.21$), and no REM-mediated modulation was observed ($t_{14} = -0.16$, $P = 0.8772$, $d = 0.04$). Moreover, these results from human hippocampus mirrored the pattern that was observed in rodent hippocampus. In contrast, frontal scalp EEG activity differed between both species likely reflects the contribution of hippocampal activity to scalp EEG in rodents (fig. S1).

In sum, these results reveal a double dissociation between the PFC and MTL REM sleep with lower aperiodic activity (steeper spectral slope) observed during neocortical REM sleep, possibly providing the optimal neurophysiological milieu to enable neuroplasticity in support of long-term memory retention (*29*).

Furthermore, our findings indicate that REM sleep resulted in a decrease in the spectral slope during subsequent NREM sleep, in line with our observations on the scalp level (cf. Fig. 3, D and E). In contrast to the neocortical reduction of the aperiodic activity during REM sleep, a switch to a higher rate of aperiodic activity (flattening of the spectral slope) was evident in the MTL, where no REM-mediated down-regulation of aperiodic activity in adjacent NREM epochs was observed.

Next, we analyzed high-frequency band (HFB) activity, a surrogate marker of multi-unit firing and dendritic synaptic potentials (*30*). Mean HFB activity only changed in MTL but not PFC over the course of the triplet (MTL: $F_{1.3,18.9} = 15.94$, $P = 0.0003$; PFC: $F_{1.5,21.7} = 0.39$, $P = 0.6279$) with no overnight modulation (both P values > 0.5) in both regions. However, we found a dispersion of activity patterns across all recording sites (Fig. 4D, last row). Population vector analysis revealed a regionally specific modulation of the multidimensional distance across the triplet (two-way RM-ANOVA; ROI: $F_{1,14} = 42.07$, $P < 0.0001$, state: $F_{1.2,16.6} = 3.77$, $P = 0.0634$; interaction: $F_{1.5,21.3} = 1.84$, $P = 0.1878$), which reflects a more heterogeneous and less synchronized population response. We again observed a modulation of population activity in NREM following REM sleep in PFC ($t_{14} = 2.50$, $P = 0.0253$, $d = 0.65$) but not in the MTL ($t_{14} = 1.24$, $P = 0.2354$, $d = 0.32$). To further quantify the REM-mediated modulation, we separately correlated the overall REM spectral slope (analogous to Fig. 3, F and G) with different sleep signatures. Collectively, this set of findings supports the hypothesis that REM-mediated aperiodic downmodulation preferentially occurs in the neocortex, a key node for human long-term memory retention (*1*).

Steeper spectral slopes (indexing decreased aperiodic activity) during REM sleep predicted increased overnight hippocampal ripple activity (Spearman rho = 0.75, $P = 0.0018$), HFB activity (rho = −0.70, $P = 0.0046$), and active periods (rho = −0.64, $P = 0.0129$; see Materials and Methods). This was observable on the individual subject level (Fig. 4E) and predicted the steepening of the spectral slope across the full night (Fig. 4E; rho = 0.68, $P = 0.0073$; replicating Fig. 3G). The same relationship between REM slope and the overnight steepening of the spectral slope was observed in PFC (Fig. 4F; rho = 0.12, $P_{\text{pseudo-population}} = 0.0277$, $P_{\text{lme}} < 0.0001$; $t_{345} = 6.72$; $CI_{95} = [0.06\ 0.11]$). In addition, the expression of spindles changed as a function of the REM slope (rho = 0.11, $P_{\text{pseudo-population}} = 0.0380$, $P_{\text{lme}} = 0.0599$; $t_{345} = -1.89$; $CI_{95} = [-0.009\ 0.0002]$), while the relationship to prefrontal SOs was less consistent (rho = −0.19, $P_{\text{pseudo-population}} = 0.0004$, $P_{\text{lme}} = 0.1012$; $t_{345} = 1.64$; $CI_{95} = [-0.001\ 0.012]$; fig. S8). The modulation of the spindle count by the REM slope exhibited an opposite pattern between medial and lateral frontal cortex, with a decrease in medial and an increase in lateral prefrontal regions (Fig. 4F; $P_{\text{lme}} = 0.0157$; $t_{345} = 2.43$; $CI_{95} = [5 \times 10^{-5}\ 5 \times 10^{-4}]$). Last, we tested whether brief oscillatory beta/gamma bursts might explain the observed effect on the spectral slope, but we did not find any evidence for this consideration (fig. S9).

Together, these results reveal that aperiodic activity during REM sleep predicts the overnight modulation of aperiodic activity, an EEG-based proxy of excitability during sleep. Critically, the post-REM modulation of successive NREM sleep was confined to the neocortex, indicating that REM-mediated aperiodic down-regulation preferentially affects neocortical regions to support long-term memory retention.

DISCUSSION

Together, our results across five independent studies demonstrate that REM sleep mediates an overnight down-regulation of aperiodic activity as quantified by the spectral slope. This REM sleep mechanism provided functional benefits, such that it predicted the success of subsequent overnight long-term memory retention, suggesting a possible mechanistic pathway that contributes to the recognized role of sleep in cementing human memories.

These results reveal that aperiodic activity during sleep indexes mesoscale population activity and reflects an inherent characteristic of the functional organization of the sleeping brain. Aperiodic activity operates in concert with sleep oscillations [and provides non-redundant information to SOs; cf. fig. S6; (*1*, *2*, *31*)] to mediate overnight memory consolidation. Our present simultaneous two-photon calcium imaging and electrophysiology experiments in rodents and humans provide evidence for the idea that aperiodic activity tracks mesoscale population dynamics as quantified by calcium activity. An important feature of aperiodic activity is that it can be estimated from the scalp or intracranial EEG for every state including wakefulness, providing an electrophysiological marker enabling a direct comparison of activity across different neural and behavioral states. Sleep deprivation, as a perturbation approach of the assumed physiologic modulation, resulted in an attenuated down-regulation of aperiodic activity. Moreover, aperiodic activity in REM sleep led to a pronounced functional and anatomical dissociation between two key brain regions of the memory network, the MTL and neocortex. Specifically, the MTL switched from a stable state of low aperiodic activity during NREM sleep to a transient state of increased aperiodic activity (flattening of the PSD) during REM sleep, while the neocortex transitioned from high aperiodic activity during NREM to a state of decreased

aperiodic activity (steeper slope) during REM sleep. In addition, aperiodic activity during REM sleep correlated with the overnight modulation of oscillatory NREM sleep signatures in a spatially specific manner, with aperiodic activity in the MTL indexing the modulation of hippocampal ripples, while neocortical aperiodic activity predicted spindle modulation. These findings indicate an important interaction between sleep stages, such that the expression of NREM sleep oscillations is governed by the preceding REM sleep episode.

Aperiodic activity tracks population dynamics during sleep

How does the sleeping brain regulate neural homeostasis to meet the demands of optimal function, including that required for information processing and memory retention? A possible hypothesis is that new synapses might be formed, existing connections strengthened and overall neural firing increased during wakefulness and learning (*5*, *6*, *32*). This activity increase might be particularly pronounced during early development (*33*) and for highly active cells (*9*). Sleep has been proposed to counteract this progressive activity build-up to maintain healthy neural functioning, with sleep deprivation attenuating such a modulation and impairing cognitive processes and memory formation (*5*, *34*, *35*).

On the cellular level, sleep reduces neural firing (*5*) and promotes synapse elimination (*6*, *32*). Electrophysiological recordings suggested that synaptic activity is strongly attenuated during "down-states," which may manifest as SOs in meso- and macroscale recordings (*36*, *37*). Hence, the seminal synaptic homeostasis hypothesis posits that SO-mediated postsynaptic depression might restore the optimal neural milieu for learning and memory (*2*, *10*), but it remains poorly understood how the regulation as observed on the cellular level relates to macroscale EEG activity as recorded from the human brain.

Computational models have proposed a missing link between cellular and macroscale signals (*15*, *16*). The present studies tested the predictions of these models that aperiodic activity indexes neural E/I balance and hence might be modulated during sleep. We observed that the spectral slope, as a measure of aperiodic activity, captured in vivo mesoscale dynamics. Specifically, higher calcium activity, which indexes neural population activity (*18*), predicted increased aperiodic activity (a flattening of the EEG spectral slope; Fig. 1H), while lower calcium activity decreased aperiodic activity (steepening of the EEG spectral slope). The spectral slope also indexed the momentary ratio between pyramidal and interneuron activity (Fig. 1I); this dependence was mainly observed when calcium activity was low. In contrast to the model predictions, a surplus of pyramidal cell activity (fourth E/I quartile; Fig. 1J) was accompanied by a steepening of the spectral slope. This deviation from the model predictions might be explained by the absence of recurrent connections between excitatory and inhibitory cells in the original model by Gao *et al.* (*15*), which constitutes a hallmark of neocortical circuits in vivo (Fig. 1, E and F). Moreover, all calcium recordings were obtained from cortical layers 2/3 cell soma; hence, future experiments have to determine whether these results generalize to the synaptic level or other cortical layers (*38*). Likewise, the contribution of dendritic potentials needs to be considered in future experiments. Since the current findings were obtained using calcium activity as a surrogate of neural activity (*18*), the present results need to be extended using direct electrophysiological unit recordings. Collectively, this set of findings demonstrates that the spectral slope, as an index of aperiodic brain activity, captures neural excitability at the mesoscale (defined as overall pyramidal calcium activity) and only indirectly the underlying balance between excitatory pyramidal cell and inhibitory interneuron activity. To date, the relative contributions of synaptic currents and neural firing to generation of the EEG remains incompletely understood (*39*). Future computational models accounting for recurrent connections might be able to separate the relative contributions of neural firing and momentary E/I ratio. In the same vein, future studies need to determine how other factors, such as cerebral blood, cerebrospinal, or interstitial fluid flow, glymphatic flow, or the effects of neuro-modulatory systems, affect aperiodic activity.

While sleep decreased aperiodic activity (steeper slope), sleep deprivation attenuated increased aperiodic activity (flatter slope). The strongest decrease of neocortical aperiodic activity (and cortical pyramidal cell activity in rodents; Fig. 1B) was observed during REM sleep. This observation raises the intriguing question of whether REM sleep mediates the overnight recalibration of EEG-based markers of neural excitability in humans.

REM sleep recalibrates neural activity dynamics during sleep

While SOs during NREM sleep have typically been linked to neural quiescence (*40*), mounting evidence suggests that such NREM sleep consequences are nuanced and that NREM sleep also reflects a brain state of considerable activity (*1*, *9*, *41*). For example, NREM sleep may increase synaptic efficiency (*42*), especially for small synaptic boutons (*2*), and neural firing (*9*) (pronounced for low firing neurons) at the cellular level (*1*). At the population level, the cardinal oscillations of NREM sleep actively coordinate the hippocampal-neocortical dialogue to enable information reactivation, transfer, and consolidation (*1*, *43*). NREM sleep oscillations, including sharp-wave ripples, which are typically nested in SOs or spindles (*44*–*46*), have been suggested to mediate neuroplasticity through repetitive replay of firing sequences (*43*, *47*) and the memory-specific up-regulation of synapse formation (*48*); thus, reflecting a potential state of increased net excitation, in addition to co-occurring benefits of synaptic downscaling (*2*, *10*).

In contrast, emerging evidence in animal models indicates a role for a neuronal inhibitory state in REM sleep (*37*). At a cellular level, REM sleep promotes global synapse elimination (*11*, *12*). Moreover, two-photon calcium imaging (*21*) (cf. Fig. 1) and in vivo electrophysiology studies (*8*, *9*) report a global reduction of neural firing with an increase of interneuron activity during REM sleep. This is in accord with macroscale findings that demonstrated a reduction of aperiodic activity, possibly reflecting decreased population excitability in scalp EEG recordings (*14*). The present results provide direct in vivo evidence corroborating this proposal in human cortex, showing that REM-mediated activity modulates neural dynamics of the brain during this sleep state (*8*, *9*, *29*, *49*). This modulation was both region– (MTL versus PFC; Fig. 4 and figs. S1 and S7) and species- (human versus rodent; fig. S1)–specific. In both species, we observed a flattening of spectral slope during REM sleep in the hippocampus, highlighting that hippocampal brain state–dependent dynamics might be evolutionary conserved (*50*). In contrast, the strongest REM-mediated aperiodic modulation was observed in human frontal cortex. This effect was not evident in rodents, where frontal EEG activity also encompasses the contribution of hippocampal activity (fig. S1), which directly accounts for the apparent inconsistency between both species. Moreover,

previous work in rodent (*51*), cat (*52*), and human (*41*) visual cortex observed that NREM sleep potentiates neural excitability (*51*, *52*) and increases E/I balance in V1 (defined by magnetic resonance spectroscopy as the glutamate to γ-aminobutyric acid ratio) (*41*) to possibly promote neural plasticity. Critically, no sleep-mediated downscaling was observed in visual cortex (*51*, *52*). These observations are in line with the present findings where the most pronounced and behaviorally relevant modulation of aperiodic activity occurred over frontocentral areas (Figs. 2C and 3I), while the aperiodic modulation over occipital sensors was negligible (Fig. 3, D, F, and G).

REM sleep–mediated recalibration of aperiodic activity predicts memory retention

Is the change in aperiodic activity during REM sleep epiphenomenal or functional, specifically regarding sleep-dependent overnight memory processing (*7*)? At the cellular level, consolidation of mnemonic representations requires a selective, activity-dependent elimination of synapses (*10*). As this down-scaling occurs primarily in sleep, prolonged wakefulness is proposed to result in synapse saturation leading to impaired memory function (*5*, *53*).

Consistent with this proposition, when interneurons in hippocampus are optogenetically inactivated during REM sleep in rodents, memory formation is impaired (*54*). Conversely, REM sleep deprivation in rodents reduced synaptic plasticity (*55*). This set of findings suggests a role for REM sleep in adjusting neural activity overnight in support of memory retention. This recalibration had a functional benefit predicting successful next day memory retention. This association with memory enhancement was specific to the PFC, in line with the idea that neocortical areas house long-term mnemonic storage (*28*). This effect was not confounded by the simultaneously influence of slow wave activity on behavior (fig. S6), suggesting that aperiodic and slow wave activity constitute complementary mechanisms.

Collectively, our study provides compelling evidence that aperiodic electrical brain activity within the human and rodent brain serves as a reliable indicator of neural population dynamics. Hence, aperiodic activity represents an essential and previously unrecognized functional characteristic of the sleeping brain. These findings shed light on the pivotal role of human REM sleep in recalibrating neural dynamics at the population level. Our results illustrate that the recalibration of population-based excitability markers facilitated by REM sleep not only supports but also potentially stems from experience-dependent plasticity throughout the waking hours. In sum, REM-mediated recalibration of neural dynamic might be critical for the overnight consolidation of memories into stable engrams within the brain.

MATERIALS AND METHODS

Participants

Study 1: Two different strains of transgenic mice, PV-Cre mice (RRID:IMSR_JAX:008069; n = 4) and SOM-Cre mice (RRID: IMSR_JAX:013044; n = 4) were used. All mice were housed in groups of up to five animals under temperature-controlled and humidity-controlled conditions (22° ± 2°C; 45 to 65%) and a 12-hour/12-hour light/dark cycle. All recordings started during the first hour of the light phase, and only male mice older than 8 weeks were recorded. Procedures and data were the same as described previously (*21*, *56*). All experiments were approved by the local institutions in charge of animal welfare (CIN4/11. Regierungspräsidium Tübingen, State of Baden-Wuerttemberg, Germany).

Study S1: The recordings were performed in five male Long Evans rats (Janvier, Le Genest-Saint-Isle, France, 280 to 340 g, 14 to 18 weeks old). Animals were kept on a 12-hour/12-hour light/dark cycle with lights off at 19:00 hours. Water and food were available ad libitum. All experiments were approved by the local institutions in charge of animal welfare (MPV3/13, Regierungspräsidium Tübingen, State of Baden-Wuerttemberg, Germany). Procedures and data were the same as described previously (*57*, *58*).

Study 2: Fourteen younger (20.6 ± 2.2 years; mean ± SD) and 26 healthy older adults (73.0 ± 5.4 years; mean ± SD) participated in the study. Neurobehavioral correlations were highly comparable (see fig. S3). All participants provided written informed consent according to the local ethics committee (Berkeley Committee for Protection of Human Subjects Protocol Number 2010-01-595) and the Sixth Declaration of Helsinki. Here, we report a subset of participants from a larger cohort that also completed three resting state recordings in addition to overnight sleep recordings, which were unavailable for remainder of the participants (*23*, *24*).

Study 3: Twelve young healthy controls (mean age: 23.2 ± 1.1 years; seven men, five women) participated in the study. All participants provided written informed consent according to the local ethics committee at the University of Mannheim (protocol number 2010-311 N-MA) and the Sixth Declaration of Helsinki. The resting state data were acquired in the context of a larger study investigating the effects of sleep deprivation on habituation but have not been reported previously (*59*).

Study 4: We obtained intracranial recordings from 15 pharmacoresistant epilepsy patients (35.0 ± 11.1 years; mean ± SD; nine females) who underwent presurgical monitoring with implanted depth electrodes (Ad-Tech), which were placed stereo-tactically to localize the seizure onset zone. All patients were recruited from the University of California Irvine Medical Center, USA. Electrode placement was exclusively dictated by clinical considerations, and all patients provided written informed consent to participate in the study. Patients selection was based on magnetic resonance imaging (MRI)–confirmed electrode placement in the MTL and PFC from a larger cohort of 21 subjects (*14*, *45*). We only included patients where one seizure free night was available and a sufficient amount of REM sleep was recorded (see inclusion criteria below; two subjects did not exhibit simultaneous MTL and PFC coverage; four subjects did not exhibit sufficient REM sleep). The study was not preregistered. All procedures were approved by the Institutional Review Board at the University of California, Irvine (protocol number: 2014-1522) and conducted in accordance with the Sixth Declaration of Helsinki.

Experimental design and procedure

Study 1: All animals were anesthetized with ketamine (0.1 mg/g) and xylazine (0.008 mg/g) with a supplement of isoflurane. For topical anesthesia, lidocaine was applied. Afterward, the animals were mounted on a stereotaxic frame. Body temperature was continuously monitored and maintained at 37°C. A custom-made headpost was glued to the skull and subsequently cemented with dental acrylic (Kulzer Palapress). Virus injection and the implantation of the imaging window followed headpost implantation. To this end, a craniotomy above the sensorimotor cortex (1.1 mm caudal

and 1 to 1.3 mm lateral from the bregma) with a size of 1.2 × 2 mm was made. Afterward, two viruses (AAV2/1-syn-GCaMP6f 2.96 × 10^{12} genomes/ml and AAV2/1-Flex- tdTomato 1.48 × 10^{11} genomes/ml) were injected into multiple sites of the area of craniotomy (10 to 20 nl per site; 3 to 5 min per injection). The injection depth was between 130 and 300 mm. Virus injection was followed by the implantation of the imaging window (1 × 1.5 mm). The space between the skull and the imaging window was filled with agarose (1.5 to 2%), and then the imaging window was cemented with dental acrylic. EEG electrodes were implanted on the cortical surface of the contralateral hemisphere relative to the imaging window (−2.5 mm, lateral +2.5 mm from bregma). The reference electrodes were implanted on the brain surface 1 mm relative to lambda. Two wire electrodes were implanted into the neck muscle for EMG recordings (Science Products). After the surgery, all animals were brought back to their home cage and were single-housed for the rest of the experiments. They had at least 10 days of recovery from surgery before imaging sessions started. After handling the animals 10 min/day for 1 week, the animal was habituated to the head fixation. Habituation consisted of four sessions per day for 1 week with increasing fixation durations (30 s, 3 min, 10 min, and 30 min) interleaved by 10-min rest intervals. Habituation was conducted until 24 hours before the first imaging session during the early light phase.

Study S1: Animals were anesthetized with an intraperitoneal injection of fentanyl (0.005 mg/kg of body weight), midazolam (2.0 mg/kg), and medetomidine (0.15 mg/kg). They were placed into a stereotaxic frame and were supplemented with isoflurane (0.5%) if necessary. The scalp was exposed and five holes were drilled into the skull. Three EEG screw electrodes were implanted: one frontal electrode [anteroposterior (AP): +2.6 mm, mediolateral (ML): −1.5 mm, with reference to bregma], one parietal electrode (AP: −2.0 mm, ML: −2.5 mm), and one occipital reference electrode (AP: −10.0 mm, ML: 0.0 mm). In addition, a platinum electrode was implanted into the right dorsal hippocampus [AP: −3.1 mm, ML: +3.0 mm, dorsoventral (DV): −3.6 mm]. Electrode positions were confirmed by histological analysis. One stainless steel wire electrode was implanted in the neck muscle for EMG recordings. Electrodes were connected to an electrode pedestal (PlasticsOne, USA) and fixed with cold polymerizing dental resin, and the wound was sutured. Rats had at least 5 days for recovery.

Study 2: All participants were trained on the episodic word-pair task in the evening and performed a short recognition test after 10 min. Then, participants were offered an 8-hour sleep opportunity, starting at their habitual bedtime (table S1). Resting state recordings were obtained directly before and after sleep. Polysomnography was collected continuously. Participants performed a long version of the recognition test approximately 2 hours after awakening. Subsequently, we obtained structural MRI scans from all participants. Two older adults did not complete behavioral testing, and two young adults failed to achieve criterion at encoding. Thus, these four subjects were excluded from behavioral analyses but were included in all electrophysiological analyses.

Study 3: In the 3 days before the experiment, sleep was monitored using an Actiwatch Device (Philips Respironics, Amsterdam). Participants were randomly assigned to either start in the sleep deprivation or habitual sleep group. In the experimental night, participants were either allowed to sleep and monitored using the Actiwatch device or kept awake and engaged by an experimenter. Recordings were obtained in the late AM or around noon.

Study 4: We recorded a full night of sleep for every participant. Recordings typically started around 8:00 to 10:00 p.m. and lasted for ~10 to 12 hours (table S2). Only nights that were seizure-free were included in the analysis. Polysomnography was collected continuously.

Behavioral task

Study 2: We used a previously established sleep-dependent episodic memory task (Fig. 2B), where subjects had to learn word-nonsense word pairs (*23*). Briefly, words were 3 to 8 letters in length and drawn from a normative set of English words, while nonsense words were 6 to 14 letters in length and derived from groups of common phonemes. During encoding, subjects learned 120 word-nonsense pairs. Each pair was presented for 5 s. Participants performed the criterion training immediately after encoding. The word was presented along with the previously learned nonsense word and two new nonsense words. Subjects had to choose the correctly associated nonsense words and received feedback afterward. Incorrect trials were repeated after a variable interval and were presented with two additional new nonsense words to avoid repetition of incorrect nonsense words. Criterion training continued until correct responses were observed for all trials.

During recognition, a probe word or a new (foil) probe word was presented along with four options: (i) the originally paired nonsense word, (ii) a previously displayed nonsense word, which was linked to a different probe (lure), (iii) a new nonsense word, or (iv) an option to indicate that the probe is new. During the recognition test after a short delay (10 min), 30 probe and 15 foil trials were presented. At the long delay (10 hours), 90 probe and 45 foil trials were tested. All probe words were presented only once during recognition testing, either during short or long delay testing.

Sleep monitoring and EEG data acquisition

Study 1: Sleep stages were identified on the basis of EEG and EMG recordings during the imaging sessions. EEG and EMG signals were amplified, filtered (EEG: 0.01 to 300 Hz; EMG: 30 to 300 Hz), and sampled at a rate of 1000 Hz (Grass Technologies amplifier, model 15A54). On the basis of EEG/EMG signals for succeeding 10-s epochs, the brain state of the mouse was classified into wake, slow-wave sleep, and REM sleep stages. Sleep stages were determined with the software SleepSign for animals (Kissei Comtech).

Study S1: Rats were habituated to the recording box [dark gray polyvinyl chloride (PVC), 30 cm by 30 cm, height: 40 cm] for 2 days, 12 hours/day. On the third day, animals were recorded for 12 hours, during the light phase, starting at 7:00 hours. The animal′s behavior was continuously tracked using a video camera mounted on the recording box. EEG, local field potential (LFP), and EMG signals were continuously recorded and digitalized using a CED Power 1401 converter and Spike2 software (Cambridge Electronic Design). During the recordings, the electrodes were connected through a swiveling commutator to an amplifier (Model 15A54, Grass Technologies). The screw electrode in the occipital skull served as reference for all EEG, LFP, and EMG recordings. Filtering was for the EEG between 0.1 and 300 Hz; for LFP signals, a high-pass filter of 0.1 Hz was applied; and for the EMG between 30 and 300 Hz, signals were sampled at 1 kHz.

Study 2: Polysomnography sleep monitoring was recorded on a Grass Technologies Comet XL system (Astro-Med), including 19-channel EEG placed using the standard 10-20 system as well as electromyography (EMG). Electrooculogram (EOG) was recorded the right and left outer canthi. EEG recordings were referenced to bilateral linked mastoids and digitized at 400 Hz. Sleep scoring was performed according to standard criteria by Rechtschaffen and Kales in 30-s epochs (*60*). NREM sleep was defined as NREM stages 2 to 4. First and last NREM and REM epochs were defined as the first and last 5 min of the respective stages in the hypnogram.

Study 3: Resting state EEG recordings were obtained using a 64-channel BrainAmp amplifier (Brain Products GmbH) EEG system with equidistant Ag-AgCl electrode positions (EasyCap, Herrsching, Germany). The central electrode of this layout corresponded to electrode Cz (10–20 layout) and was therefore used for between group comparisons.

Study 4: We recorded from all available intracranial electrodes. To facilitate sleep staging based on established criteria, we also recorded scalp EEG, which typically included recordings from electrodes Fz, Cz, C3, C4, and Oz according to the international 10-20 system. EOG was recorded from four electrodes, which were placed around the right and left outer canthi. All electrophysiological data were acquired using a 256-channel Nihon Kohden recording system (model JE120A), analog-filtered at 0.01 Hz, and digitally sampled at 5000 Hz. All available artifact-free scalp electrodes were low-pass–filtered at 50 Hz, demeaned and detrended, downsampled to 400 Hz, and referenced against the average of all clean scalp electrodes. EOGs were typically bipolar referenced to obtain one signal per eye. A surrogate EMG signal was derived from electrodes in immediate proximity to neck or skeletal muscles, by high-pass filtering either the ECG or EEG channels above 40 Hz. Sleep staging was carried out according to Rechtschaffen and Kales guidelines by trained personnel in 30-s segments (*60*) as reported previously (*23*, *24*). Same conventions as in study 1 were used.

Two-photon calcium imaging data acquisition

Study 1: In vivo imaging was performed using a two-photon microscope based on the MOM system (Sutter) controlled by ScanImage software (*61*). The light source was a pulsed Ti:sapphire laser (l = 980 nm; Chameleon; Coherent). Red and green fluorescence photons were collected with an objective lens (Nikon; 16×; 0.80 numerical aperture), separated by a 565-nm dichroic mirror (Chroma; 565dcxr) and barrier filters (green: ET525/70 m-2p; red: ET605/70 m- 2p), and measured using photomultiplier tubes (Hamamatsu Photonics; H10770PA-40). Imaging frames were visually inspected to exclude cross-talk between green and red channels. The imaging frame consisted of 1024 × 256 pixels, and the frame rate was 5.92 Hz (169 ms per frame). Images were collected in layer 2/3 at a depth of 150 to 250 mm.

CT and MRI data acquisition

Study 4: We obtained anonymized postoperative computed tomography (CT) scans and presurgical MRI scans, which were routinely acquired during clinical care. MRI scans were typically 1 mm isotropic.

Quantification and statistical analysis

Behavioral data analysis

Study 2: Memory recognition was calculated by subtracting both the false alarm rate (proportion of foil words, which subjects reported as previously encountered) and the lure rate (proportion of words that were paired with a familiar but incorrect nonsense word) from the hit rate (correctly paired word-nonsense word pairs). Memory retention was subsequently calculated as the difference between recognition at long minus short delays.

Two-photon data

Preprocessing and data analysis

Image analysis: Lateral motion was corrected in two steps. A cross-correlation–based image alignment (Turboreg) was performed, followed by a line-by-line correction using an algorithm based on a hidden Markov model (*62*). ROIs containing individual neurons were drawn manually, and the pixel values within each ROI were summed to estimate the fluorescence of this neuron. PV^+ and SOM^+ were manually detected by red fluorescence signal expressed by AAV2/1-Flex-tdtomato. The individual cell traces were calculated as the average pixel intensity within the ROIs for each frame. The cell traces were transformed into the percent signal change ($\Delta F/F$), in which the baseline for each cell was defined as the 20th percentile value of all frames within a ±3-min interval. We then extracted active frames ("calcium spikes"), which were defined as frames with $\Delta F/F$ signals two SDs above the mean in a sliding time window of ±3 min.

To confirm that the neuropil signal did not affect our results and to compensate for background noise, we performed a standard neuropil subtraction for each cell's fluorescence trace. The neuropil signal was estimated for each ROI as the average pixel value within two pixels around the ROI (excluding adjacent cells). The true signal was estimated as $F(t)$ = FinROI − r × FaroundROI, where r = 0.7.

Immunohistochemistry

After finishing the experiments, mice were deeply anesthetized [ketamine (0.3 mg/g) and xylazine (0.024 mg/g), i.p.] and with 4% paraformaldehyde (PFA) in 0.1 M phosphate-buffered saline (PBS) intracardially perfused. Then, the brains were postfixed in 4% PFA at 4°C overnight and rinsed three times with 0.1 M PBS. Coronal slices (thickness, 65 mm) were blocked in 10% normal goat serum (NGS; Jackson ImmnunoResearch) and 0.3% Triton X-100 (Sigma-Aldrich) in 0.1 M PBS for 1.5 hours at room temperature. Slices were incubated with anti-PV rabbit primary antibody (1:1000; #24428, Immunostar, RRID: AB_572259) or anti-SOM rabbit primary antibody (1:1000; #T-4547, Peninsula Laboratories, RRID: AB_518618) in carrier solution (2% NGS and 0.3% Triton X-100 in PBS) for 48 hours at 4°C. Following 4× 10-min rinses with 0.1 M PBS, the slices were incubated in goat anti-rabbit immunoglobulin G antibodies conjugated either with Alexa Fluor 405 (for PV^+ staining, AB_221605) or Alexa Fluor 633 (for SOM^+ staining, AB2535732; both from Thermo Fisher Scientific; 1:1000) in carrier solution for 3 hours at room temperature on the shaker. Images were acquired on a confocal microscope (LSM 710, Carl Zeiss). Overall, the fraction of cells only expressing Alexa Fluor but not tdtomato and GCamp6f for PV^+ and SOM^+ was each below 2%.

EEG data

Preprocessing

Study 1: EEG data from a frontal and parietal electrode were imported into MATLAB analyzed using the FieldTrip toolbox. Raw recordings were demeaned, detrended, and epoched into 10-s segments. Epochs containing artifacts were labeled semi-automatically when a threshold of 6 SD was exceeded in the concurrently acquired EMG signal. Data were referenced to a bipolar pair (frontal-parietal) for selected analyses (e.g., fig. S1).

Study S1: EEG data from a frontal and parietal electrode as well as a hippocampal electrode were imported into MATLAB analyzed using the FieldTrip toolbox. Raw recordings were demeaned, detrended, and epoched into 10-s segments. Data were referenced to a bipolar pair (frontal-parietal) for selected analyses (e.g., fig. S1).

Study 2/3—Resting state: EEG data were imported into MATLAB and analyzed using the FieldTrip toolbox. Raw recordings were demeaned, detrended, high-pass–filtered at 1 Hz, common average referenced, and epoched into 3-s-long segments with 50% overlap. Artifact detection was done semi-automatically for EOG, jump, and muscle artifacts and visually confirmed (*63*).

Study 2—Sleep: EEG data were imported into FieldTrip, then demeaned, detrended, common average referenced, and epoched into non-overlapping 30-s segments. Artifact detection was done manually in 5-s segments (*24*).

Study 4: Scalp EEG was demeaned, detrended, and locally referenced against the mean of all available artifact-free scalp electrodes. We applied a 50-Hz low-pass filter and down-sampled the data to 500 Hz. All scalp EEG analyses were done on electrode Fz. In a subset of subjects, Fz was not available and Cz was used instead of Fz. Intracranial EEG: In every subject, we selected all available electrodes in the MTL, which were then demeaned, detrended, notch-filtered at 60 Hz and its harmonics, bipolar referenced to its immediate lateral neighboring electrode, and lastly down-sampled to 500 Hz. We retained all MTL channels but discarded noisy PFC channels. We adopted a previously introduced approach where we first detected interictal epileptic discharges (IEDs) using automated detectors (see below), which were then excluded from further analysis. Last, we selected one MTL electrode per participant with the lowest number of overall detections. For PFC analyses, all available contacts in these regions were included, and the same preprocessing steps were applied. Then, all resulting traces were manually inspected, and noisy, epileptic, and artifact-contaminated PFC channels were excluded.

Extraction of REM epochs and time normalization procedure

Study 1: Sleep data were manually staged. REM epochs were detected on the basis of the emergence of a prominent theta rhythm (4 to 10 Hz) and reduction of EMG activity. Given that a NREM-REM-NREM triplet analysis was not feasible (see fig. S2), we selected *N* continuous REM epoch that spanned at least three 10-s epochs and included ±*N* adjacent epochs (termed pre-REM, mostly NREM and post-REM, mostly wake). This ensured that an equal amount of data was included to assess the relationship of population dynamics and aperiodic activity. The values within every epoch were then averaged into one composite value for calcium and EEG activity.

Study3/4: REM epochs were detected on the basis of the manually staged hypnogram according to established Rechtschaffen and Kales guidelines (*60*). We first detected all REM epochs and then selected artifact-free epochs that spanned at least three consecutive epochs (90 s) and required that the majority of adjacent periods within a time window ±9 min were staged as NREM sleep (9 min were chosen to match the 9 min of resting state data reported in Fig. 2A as well as to match the average, artifact- and interruption-free duration of individual NREM epochs: study 3: 10 ± 13.9 min; study 4: 7 ± 16.7 min; median ± SD). Subsequently, the identified REM epochs were extracted as continuous time-domain signals and then epoched into 100 overlapping epochs and subjected to multitaper spectral analysis as outlined below. Similarly, the adjacent NREM data were epoched into 10-s-long segments with 70% overlap. The spectral estimates were then concatenated to form the final time-normalized triplet in the frequency domain. For statistical testing, we omitted the transition states and selected one third of the time-normalized epoch (beginning, center, and end of the triplet, respectively) for subsequent testing. We also repeated the entire analysis on more liberal criteria (fig. S5; inclusion of brief epochs of NREM1 or microarousals as well as episodes that were staging was uncertain) as outlined by Watson *et al.* (*9*). Here, the preceding and following NREM epochs were also time-normalized (in contrast to taking a fixed window) into 100 overlapping epochs and subjected to multitaper spectral analysis. In addition, we extracted time-normalized NREM epochs where continuous NREM epochs were equally epoched into 100 overlapping segments (figs. S5G and S7C).

Spectral analysis

Scalp EEG (studies 1, S1, and 2 to 4): Resting state spectral estimates were obtained through multitaper spectral analyses (*64*, *65*), based on discrete prolate slepian sequences. Spectral estimates were obtained between 1 and 50 Hz in 1-Hz steps. We adapted the number of tapers to obtain a frequency smoothing of ±2 Hz. For studies 1 and S1, we used an upper cutoff of 35 Hz given a broad hardware notch filter artifact from 40 to 60 Hz.

Intracranial EEG (study 4): Spectral estimates were by means of multitaper spectral analyses based on discrete prolate spheroidal sequences in 153 logarithmically spaced bins between 0.25 and 181 Hz (*64*). We adjusted the temporal and spectral smoothing to approximately match a ±2-Hz frequency smoothing.

Estimation of aperiodic background activity

Aperiodic activity was estimated from three parameters of the electrophysiological power spectrum: spectral slope x (the negative exponent of the $1/f^x$ decay function), y intercept, and the population time constant (the frequency where a bend/"knee" occurs in the $1/f$ spectrum). Note that the slope and y intercept provided redundant information (correlated at rho = −0.98, $P < 0.0001$; Spearman correlation), thus, analyses focused on the spectral slope.

FOOOF fitting: To obtain estimates of aperiodic background activity, we first used the FOOOF algorithm (*66*). EEG spectra were fitted in the range from 1 to 45 Hz. Aperiodic background activity was defined by its slope parameter χ, the y intercept c, and a constant k (reflecting the knee parameter).

$$\text{aperiodic fit} = 10^{c*} \frac{1}{(k + f^{\frac{1}{\chi}})}$$

The relationship of the knee parameter and the knee frequency is given by

$$\text{knee frequency} = k^{\frac{1}{\chi}}$$

If a knee parameter could not be determined, then we refitted the spectrum in the fixed mode, which is equivalent to a linear fit where $k = 0$.

Polynomial fitting: To estimate the spectral slope in different frequency bands, we also used first-degree polynomial fitting (*14*), thus yielding an instantaneous spectral exponent (slope, χ) and offset (*y*-axis intercept, *c*), for a given fitting range. EEG spectra were fitted using variable endpoints (from 1 to 5 to 45 Hz, 5-Hz steps), variable starting points (to 45 Hz, from 5 to 40 Hz, 5-Hz steps), a fixed bandwidth with varying center frequencies (5 to 45 Hz; ± 5 Hz), or in comparable ranges (e.g., 20 to 45 Hz; correlation to FOOOF estimates rho = 0.99, $P < 0.0001$; Spearman correlation). Typically, we report the spectral slope as obtained from the FOOOF model when fitted up to 45 Hz. In several instances, this approach was complemented by first-degree polynomial fitting to avoid high-frequency artifacts (e.g., in studies 1 and S1 from ~40 Hz; hence, we restricted the fitting up to 35 Hz), the presence of a variable spectral knee (bend of the power spectrum) or to highlight a specific frequency range in intracranial EEG, where the spectrum was estimated up to 180 Hz; hence, rendering a direct comparison of FOOOF iEEG and EEG estimates impractical. After the initial principled approach, we empirically determined the range with the highest correlation to behavior (fig. S3E; 25 to 45 Hz) and consequently used this range for all subsequent analyses.

Event detection

SOs: Event detection was performed for every channel separately based on previously established algorithms (*24*, *44*). We first filtered the continuous signal between 0.16 and 1.25 Hz and detected all the zero crossings. Then, events were selected on the basis of time (0.8- to 2-s duration) and amplitude (75% percentile) criteria. Last, we extracted 5-s-long segments (±2.5 s centered on the trough) from the raw signal and discarded all events that occurred during an IED.

Sleep spindles: On the basis of established algorithms (*24*, *44*), we filtered the signal between 12 and 16 Hz and extracted the analytical amplitude after applying a Hilbert transform. We smoothed the amplitude with a 200-ms moving average. Then, the amplitude was thresholded at the 75% percentile (amplitude criterion), and only events that exceeded the threshold for 0.5 to 3 s (time criterion) were accepted. Events were defined as sleep spindle peak-locked 5-s-long epochs (±2.5 s centered on the spindle peak).

Ripples: The signal was first filtered in the range from 80 to 120 Hz, and the analytical amplitude was extracted from a Hilbert transform in accordance with previously reported detection algorithms (*44*, *45*). The analytical signal was smoothed with a 100-ms window and *z*-scored. Candidate events were identified as epochs exceeding a *z*-score of 2 for at least 25 ms and a maximum of 200 ms and had to be spaced by at least 500 ms. We determined the instantaneous ripple frequency by detecting all peaks within the identified segment. The identified events were time-locked to the ripple trough in a time window of ±0.5 s. Overlapping epochs were merged. Epochs that contained IEDs or sharp transients were discarded.

Beta/Gamma burst detection: For fig. S9, we detected individual bursts in the range from 25 to 45 Hz, where the spectral slope was estimated, using the procedure outlined here (*67*). Briefly, we segmented the continuous LFP signal into 30-s trials and obtained single-trial spectral estimates between 1 and 50 Hz in 0.5-Hz steps with a frequency smoothing of 4 Hz. Oscillatory bursts were identified per trial by thresholding (mean ± 2 SD) the average, *z*-normalized spectral power for the frequency band of interest (25–45 Hz) relative to the mean, and SD over a reference period of 10 trials (current trial plus subsequent nine). Only bursts with a minimum duration of three oscillatory cycles of the mean frequency of interest were considered. A two-dimensional Gaussian was subsequently fitted to the time-frequency map. Burst duration was determined by the time wherein the average power for the frequency band of interest exceeded half of the local maximum as determined by the local Gaussian fit. Burst frequency was determined by the peak in the Gaussian fit. Oscillatory bursts that coincided with interictal epileptiform discharges (±1 s) relative to the burst peak were omitted. Subsequently, we obtained a burst rate per 30-s segment for every participant and channel separately. On the individual subject and channel levels, we calculated the correlation coefficient between the PSD slope and the burst rate across the entire night. We used a random block-swap procedure (1000 times; random breakpoint and block swap of the slope vector) to obtain a surrogate distribution. Subsequently, we normalized the observed correlation coefficient relative to the surrogate distribution to obtain a z-value.

IED detection: We detected IEDs using automated algorithms on all channels located in the MTL. All cutoffs were chosen in accordance with recently published findings (*44*, *68*) and were confirmed by a neurologist who visually verified the detected events. The continuous signal was filtered front and backward between 25 and 80 Hz, and the analytical amplitude was extracted from the Hilbert transform and then *z*-scored. Events were detected when this signal was 3 SD above the mean for more than 20 ms and less than 100 ms.

HFB, population activity, and active periods analysis: The HFB activity is typically defined from 70 to 180 Hz (*30*). To avoid confounding true HFB activity with ripple-band activity (upper cutoff, ~120 Hz), we defined HFB activity as the average power in this frequency range from 120 to 180 Hz. The multitaper spectral estimates where averaged into a single trace per electrode. The dynamics of the population activity were expressed as a population vector (*69*). At every time point, HFB activity was represented as a point *P* in a *n*-dimensional coordinate system where *n* reflects the number of electrodes. The population vector was then constructed by taking the Euclidean distance *d* between adjacent time points within in a given ROI, hence providing a single time course per ROI.

$$\mathrm{MDD} = d(P_t^n, P_{t+1}^n)$$

Active periods were defined as epochs where the smoothed (100-ms window) HFB signal exceeded a *z*-score of 1 for at least 50 ms (*8*).

Functional connectivity was calculated by means of the absolute of the imaginary coherency (*70*) to control for spurious coupling arising from volume conduction effects. Before connectivity analysis, time-domain data was re-referenced to pairs that did not share a common reference (hippocampal contacts to occipital bone/scalp electrode versus a bipolar scalp pair, e.g., Fz-Cz). To avoid biased connectivity estimates, 1-s segments were randomly subsampled and stratified across different states (wake, NREM, and REM) to equate the trial numbers before connectivity analysis.

Statistical analysis

Unless stated otherwise, we used cluster-based permutation tests (*71*) to correct for multiple comparisons as implemented in

FieldTrip (Monte Carlo method; 1000 iterations). Clusters were formed in time/frequency (e.g., Fig. 2) or space (e.g., Fig. 3) by thresholding two-tailed, dependent t tests or linear correlations at $P < 0.05$. Correlation values were transformed into t values using the following formula

$$t = \frac{r^* \sqrt{N-2}}{\sqrt{1-r^2}}$$

A permutation distribution was then created by randomly shuffling condition labels (paired t tests) or subject labels (correlation). The permutation P value was obtained by comparing the cluster statistic to the random permutation distribution. The clusters were considered significant at $P < 0.05$ (two-sided).

Effect sizes were quantified by means of Cohen's d or the correlation coefficient rho. To obtain effect sizes for cluster tests, we calculated the effect size separately for all channel, frequency, and/or time points and averaged across all data points in the cluster. Repeated-measures ANOVAs were Greenhouse-Geisser–corrected. For rodent data (Fig. 1) and for intracranial EEG (Fig. 4), we either averaged multiple observation per participant into one composite metric, which was then subjected to regular t tests, ANOVAs, or correlations analyses, or we used LME models with subjects as random intercepts. P values were calculated on the pseudo-population and confirmed using LME models with subjects as random intercepts.

Supplementary Materials

This PDF file includes:

Figs. S1 to S9
Tables S1 and S2

REFERENCES AND NOTES

1. J. G. Klinzing, N. Niethard, J. Born, Mechanisms of systems memory consolidation during sleep. *Nat. Neurosci.* **22**, 1598–1610 (2019).
2. G. Tononi, C. Cirelli, Sleep and the price of plasticity: From synaptic and cellular homeostasis to memory consolidation and integration. *Neuron* **81**, 12–34 (2014).
3. M. P. Walker, R. Stickgold, Sleep, memory, and plasticity. *Annu. Rev. Psychol.* **57**, 139–166 (2006).
4. G. Girardeau, V. Lopes-dos-Santos, Brain neural patterns and the memory function of sleep. *Science* **374**, 560–564 (2021).
5. V. V. Vyazovskiy, U. Olcese, Y. M. Lazimy, U. Faraguna, S. K. Esser, J. C. Williams, C. Cirelli, G. Tononi, Cortical firing and sleep homeostasis. *Neuron* **63**, 865–878 (2009).
6. V. V. Vyazovskiy, C. Cirelli, M. Pfister-Genskow, U. Faraguna, G. Tononi, Molecular and electrophysiological evidence for net synaptic potentiation in wake and depression in sleep. *Nat. Neurosci.* **11**, 200–208 (2008).
7. J. Born, G. B. Feld, Sleep to upscale, sleep to downscale: Balancing homeostasis and plasticity. *Neuron* **75**, 933–935 (2012).
8. A. D. Grosmark, K. Mizuseki, E. Pastalkova, K. Diba, G. Buzsáki, REM sleep reorganizes hippocampal excitability. *Neuron* **75**, 1001–1007 (2012).
9. B. O. Watson, D. Levenstein, J. P. Greene, J. N. Gelinas, G. Buzsáki, Network homeostasis and state dynamics of neocortical sleep. *Neuron* **90**, 839–852 (2016).
10. G. Tononi, C. Cirelli, Sleep function and synaptic homeostasis. *Sleep Med. Rev.* **10**, 49–62 (2006).
11. Y. Zhou, C. S. W. Lai, Y. Bai, W. Li, R. Zhao, G. Yang, M. G. Frank, W.-B. Gan, REM sleep promotes experience-dependent dendritic spine elimination in the mouse cortex. *Nat. Commun.* **11**, 4819 (2020).
12. W. Li, L. Ma, G. Yang, W.-B. Gan, REM sleep selectively prunes and maintains new synapses in development and learning. *Nat. Neurosci.* **20**, 427–437 (2017).
13. N. Niethard, S. Brodt, J. Born, Cell-type-specific dynamics of calcium activity in cortical circuits over the course of slow-wave sleep and rapid eye movement sleep. *J. Neurosci.* **41**, 4212–4222 (2021).
14. J. D. Lendner, R. F. Helfrich, B. A. Mander, L. Romundstad, J. J. Lin, M. P. Walker, P. G. Larsson, R. T. Knight, An electrophysiological marker of arousal level in humans. *eLife* **9**, e55092 (2020).
15. R. Gao, E. J. Peterson, B. Voytek, Inferring synaptic excitation/inhibition balance from field potentials. *Neuroimage* **158**, 70–78 (2017).
16. M. Chini, T. Pfeffer, I. Hanganu-Opatz, An increase of inhibition drives the developmental decorrelation of neural activity. *eLife* **11**, e78811 (2022).
17. B. O. Watson, M. Ding, G. Buzsáki, Temporal coupling of field potentials and action potentials in the neocortex. *Eur. J. Neurosci.* **48**, 2482–2497 (2018).
18. C. Grienberger, A. Giovannucci, W. Zeiger, C. Portera-Cailliau, Two-photon calcium imaging of neuronal activity. *Nat. Rev. Methods Primers* **2**, 67 (2022).
19. R. Boyce, S. Williams, A. Adamantidis, REM sleep and memory. *Curr. Opin. Neurobiol.* **44**, 167–177 (2017).
20. J. Ahmad, C. Ellis, R. Leech, B. Voytek, P. Garces, E. Jones, J. Buitelaar, E. Loth, F. P. Dos Santos, A. F. Amil, P. F. M. J. Verschure, D. Murphy, G. McAlonan, From mechanisms to markers: Novel noninvasive EEG proxy markers of the neural excitation and inhibition system in humans. *Transl. Psychiatry* **12**, 467 (2022).
21. N. Niethard, M. Hasegawa, T. Itokazu, C. N. Oyanedel, J. Born, T. R. Sato, Sleep-stage-specific regulation of cortical excitation and inhibition. *Curr. Biol.* **26**, 2739–2749 (2016).
22. N. Kozhemiako, D. Mylonas, J. Q. Pan, M. J. Prerau, S. Redline, S. M. Purcell, Sources of variation in the spectral slope of the sleep EEG. *Eneuro* **9**, ENEURO.0094-ENEU22.2022 (2022).
23. B. A. Mander, V. Rao, B. Lu, J. M. Saletin, J. R. Lindquist, S. Ancoli-Israel, W. Jagust, M. P. Walker, Prefrontal atrophy, disrupted NREM slow waves and impaired hippocampal-dependent memory in aging. *Nat. Neurosci.* **16**, 357–364 (2013).
24. R. F. Helfrich, B. A. Mander, W. J. Jagust, R. T. Knight, M. P. Walker, Old brains come uncoupled in sleep: Slow wave-spindle synchrony, brain atrophy, and forgetting. *Neuron* **97**, 221–230.e4 (2018).
25. M. Rudolph, M. Pospischil, I. Timofeev, A. Destexhe, Inhibition determines membrane potential dynamics and controls action potential generation in awake and sleeping cat cortex. *J. Neurosci.* **27**, 5280–5290 (2007).
26. B. Haider, M. Häusser, M. Carandini, Inhibition dominates sensory responses in the awake cortex. *Nature* **493**, 97–100 (2013).
27. V. V. Vyazovskiy, U. Olcese, E. C. Hanlon, Y. Nir, C. Cirelli, G. Tononi, Local sleep in awake rats. *Nature* **472**, 443–447 (2011).
28. P. W. Frankland, B. Bontempi, The organization of recent and remote memories. *Nat. Rev. Neurosci.* **6**, 119–130 (2005).
29. R. F. Helfrich, J. D. Lendner, R. T. Knight, Aperiodic sleep networks promote memory consolidation. *Trends Cogn. Sci.* **25**, 648–659 (2021).
30. M. Leszczyński, A. Barczak, Y. Kajikawa, I. Ulbert, A. Y. Falchier, I. Tal, S. Haegens, L. Melloni, R. T. Knight, C. E. Schroeder, Dissociation of broadband high-frequency activity and neuronal firing in the neocortex. *Sci. Adv.* **6**, eabb0977 (2020).
31. H. Miyawaki, K. Diba, Regulation of hippocampal firing by network oscillations during sleep. *Curr. Biol.* **26**, 893–902 (2016).
32. S. Maret, U. Faraguna, A. B. Nelson, C. Cirelli, G. Tononi, Sleep and waking modulate spine turnover in the adolescent mouse cortex. *Nat. Neurosci.* **14**, 1418–1420 (2011).
33. M. Jasinska, A. Grzegorczyk, O. Woznicka, E. Jasek, M. Kossut, G. Barbacka-Surowiak, J. A. Litwin, E. Pyza, Circadian rhythmicity of synapses in mouse somatosensory cortex. *Eur. J. Neurosci.* **42**, 2585–2594 (2015).
34. R. Huber, H. Mäki, M. Rosanova, S. Casarotto, P. Canali, A. G. Casali, G. Tononi, M. Massimini, Human cortical excitability increases with time awake. *Cereb. Cortex* **23**, 332–338 (2013).
35. J. T. Weiss, J. M. Donlea, Roles for sleep in neural and behavioral plasticity: Reviewing variation in the consequences of sleep loss. *Front. Behav. Neurosci.* **15**, 777799 (2022).
36. M. Steriade, A. Nuñez, F. Amzica, A novel slow (< 1 Hz) oscillation of neocortical neurons in vivo: Depolarizing and hyperpolarizing components. *J. Neurosci.* **13**, 3252–3265 (1993).
37. I. Timofeev, F. Grenier, M. Steriade, Disfacilitation and active inhibition in the neocortex during the natural sleep-wake cycle: An intracellular study. *Proc. Natl. Acad. Sci. U.S.A.* **98**, 1924–1929 (2001).
38. M. Aime, N. Calcini, M. Borsa, T. Campelo, T. Rusterholz, A. Sattin, T. Fellin, A. Adamantidis, Paradoxical somatodendritic decoupling supports cortical plasticity during REM sleep. *Science* **376**, 724–730 (2022).
39. G. Buzsáki, C. A. Anastassiou, C. Koch, The origin of extracellular fields and currents — EEG, ECoG, LFP and spikes. *Nat. Rev. Neurosci.* **13**, 407–420 (2012).
40. M. Steriade, The corticothalamic system in sleep. *Front. Biosci.* **8**, d878–d899 (2003).
41. M. Tamaki, Z. Wang, T. Barnes-Diana, D. Guo, A. V. Berard, E. Walsh, T. Watanabe, Y. Sasaki, Complementary contributions of non-REM and REM sleep to visual learning. *Nat. Neurosci.* **23**, 1150–1156 (2020).
42. S. Chauvette, J. Seigneur, I. Timofeev, Sleep oscillations in the thalamocortical system induce long-term neuronal plasticity. *Neuron* **75**, 1105–1113 (2012).

43. G. Buzsáki, Hippocampal sharp wave-ripple: A cognitive biomarker for episodic memory and planning. *Hippocampus* **25**, 1073–1188 (2015).
44. B. P. Staresina, T. O. Bergmann, M. Bonnefond, R. van der Meij, O. Jensen, L. Deuker, C. E. Elger, N. Axmacher, J. Fell, Hierarchical nesting of slow oscillations, spindles and ripples in the human hippocampus during sleep. *Nat. Neurosci.* **18**, 1679–1686 (2015).
45. R. F. Helfrich, J. D. Lendner, B. A. Mander, H. Guillen, M. Paff, L. Mnatsakanyan, S. Vadera, M. P. Walker, J. J. Lin, R. T. Knight, Bidirectional prefrontal-hippocampal dynamics organize information transfer during sleep in humans. *Nat. Commun.* **10**, 3572 (2019).
46. C.-F. V. Latchoumane, H.-V. V. Ngo, J. Born, H.-S. Shin, Thalamic spindles promote memory formation during sleep through triple phase-locking of cortical, thalamic, and hippocampal rhythms. *Neuron* **95**, 424–435.e6 (2017).
47. H. F. Ólafsdóttir, D. Bush, C. Barry, The role of hippocampal replay in memory and planning. *Curr. Biol.* **28**, R37–R50 (2018).
48. G. Yang, C. S. W. Lai, J. Cichon, L. Ma, W. Li, W.-B. Gan, Sleep promotes branch-specific formation of dendritic spines after learning. *Science* **344**, 1173–1178 (2014).
49. F. Placidi, S. Zannino, M. Albanese, A. Romigi, F. Izzi, M. G. Marciani, M. G. Palmieri, Increased cortical excitability after selective REM sleep deprivation in healthy humans: A transcranial magnetic stimulation study. *Sleep Med.* **14**, 288–292 (2013).
50. F. J. van Schalkwijk, J. Weber, M. A. Hahn, J. D. Lendner, M. Inostroza, J. J. Lin, R. F. Helfrich, An evolutionary conserved division-of-labor between hippocampal and neocortical sharp-wave ripples organizes information transfer during sleep. bioRxiv 2022.10.19.512822 (2022). https://doi.org/10.1101/2022.10.19.512822.
51. S. J. Aton, A. Suresh, C. Broussard, M. G. Frank, Sleep promotes cortical response potentiation following visual experience. *Sleep* **37**, 1163–1170 (2014).
52. M. G. Frank, N. P. Issa, M. P. Stryker, Sleep enhances plasticity in the developing visual cortex. *Neuron* **30**, 275–287 (2001).
53. M. C. D. Bridi, F.-J. Zong, X. Min, N. Luo, T. Tran, J. Qiu, D. Severin, X.-T. Zhang, G. Wang, Z.-J. Zhu, K.-W. He, A. Kirkwood, Daily oscillation of the excitation-inhibition balance in visual cortical circuits. *Neuron* **105**, 621–629.e4 (2020).
54. R. Boyce, S. D. Glasgow, S. Williams, A. Adamantidis, Causal evidence for the role of REM sleep theta rhythm in contextual memory consolidation. *Science* **352**, 812–816 (2016).
55. C. M. McDermott, M. N. Hardy, N. G. Bazan, J. C. Magee, Sleep deprivation-induced alterations in excitatory synaptic transmission in the CA1 region of the rat hippocampus. *J. Physiol.* **570**, 553–565 (2006).
56. N. Niethard, H.-V. V. Ngo, I. Ehrlich, J. Born, Cortical circuit activity underlying sleep slow oscillations and spindles. *Proc. Natl. Acad. Sci. U.S.A.* **115**, E9220–E9229 (2018).
57. C. N. Oyanedel, E. Durán, N. Niethard, M. Inostroza, J. Born, Temporal associations between sleep slow oscillations, spindles and ripples. *Eur. J. Neurosci.* **52**, 4762–4778 (2020).
58. E. Durán, C. N. Oyanedel, N. Niethard, M. Inostroza, J. Born, Sleep stage dynamics in neocortex and hippocampus. *Sleep* **41**, 10.1093/sleep/zsy060, (2018).
59. S. Schuh-Hofer, U. Baumgärtner, R.-D. Treede, Effect of sleep deprivation on the electrophysiological signature of habituation to noxious laser stimuli. *Eur. J. Pain* **19**, 1197–1209 (2015).
60. A. Rechtschaffen, A. Kales, A manual of standardized terminology, techniques, and scoring systems for sleep stages of human subjects, (Public Health Service, US Government Printing Office, Washington DC, 1968).
61. T. A. Pologruto, B. L. Sabatini, K. Svoboda, ScanImage: Flexible software for operating laser scanning microscopes. *Biomed. Eng. Online* **2**, 1–9 (2003).
62. D. A. Dombeck, A. N. Khabbaz, F. Collman, T. L. Adelman, D. W. Tank, Imaging large-scale neural activity with cellular resolution in awake, mobile mice. *Neuron* **56**, 43–57 (2007).
63. R. Oostenveld, P. Fries, E. Maris, J.-M. Schoffelen, FieldTrip: Open source software for advanced analysis of MEG, EEG, and invasive electrophysiological data. *Comput. Intell. Neurosci.* **2011**, 156869 (2011).
64. P. P. Mitra, B. Pesaran, Analysis of dynamic brain imaging data. *Biophys. J.* **76**, 691–708 (1999).
65. M. J. Prerau, R. E. Brown, M. T. Bianchi, J. M. Ellenbogen, P. L. Purdon, Sleep neurophysiological dynamics through the lens of multitaper spectral analysis. *Physiology (Bethesda)* **32**, 60–92 (2017).
66. T. Donoghue, M. Haller, E. J. Peterson, P. Varma, P. Sebastian, R. Gao, T. Noto, A. H. Lara, J. D. Wallis, R. T. Knight, A. Shestyuk, B. Voytek, Parameterizing neural power spectra into periodic and aperiodic components. *Nat. Neurosci.* **23**, 1655–1665 (2020).
67. M. Lundqvist, J. Rose, P. Herman, S. L. Brincat, T. J. Buschman, E. K. Miller, Gamma and beta bursts underlie working memory. *Neuron* **90**, 152–164 (2016).
68. J. N. Gelinas, D. Khodagholy, T. Thesen, O. Devinsky, G. Buzsáki, Interictal epileptiform discharges induce hippocampal-cortical coupling in temporal lobe epilepsy. *Nat. Med.* **22**, 641–648 (2016).
69. R. B. Ebitz, B. Y. Hayden, The population doctrine in cognitive neuroscience. *Neuron* **109**, 3055–3068 (2021).
70. G. Nolte, O. Bai, L. Wheaton, Z. Mari, S. Vorbach, M. Hallett, Identifying true brain interaction from EEG data using the imaginary part of coherency. *Clin. Neurophysiol.* **115**, 2292–2307 (2004).
71. E. Maris, R. Oostenveld, Nonparametric statistical testing of EEG- and MEG-data. *J. Neurosci. Methods* **164**, 177–190 (2007).
72. L. Petrucco, *Mouse head schema* (2020; https://zenodo.org/record/3925903).

Acknowledgments

Funding: This work was supported by German Research Foundation, Emmy Noether Program, DFG HE8329/2-1 (R.F.H.), German Research Foundation, DFG LE 3863/2-1 (J.D.L.), German Research Foundation, DFG SCHA 2369/1-1 (F.J.S.), German Research Foundation, Tr-SFB 654 (JB), German Research Foundation, EXC 307 (JB), German Research Foundation, SFB1158 Association Project (SSH, RFH), European Research Council, AdG883098 (J.B.), Hertie Foundation, Network for Excellence in Clinical Neuroscience (N.N. and R.F.H.), Jung Foundation for Research and Science, Ernst Jung Career Advancement Award in Medicine (R.F.H.), National Institutes of Health R01AG031164, RF1AG054019, and RF1AG054106 (M.P.W.), National Institute of Health 2 RO1 NS021135 (R.T.K.), and National Institutes of Health U19NS107609 (J.J.L. and R.T.K.). **Author contributions:** Conceptualization: J.D.L. and R.F.H. Methodology: J.D.L. and R.F.H. Investigation: J.D.L., N.N., B.A.M., F.J.S., S.S.-H., H.S., R.T.K., J.B., M.P.W., J.J.L., and R.F.H. Visualization: J.D.L. and R.F.H. Funding acquisition: R.T.K., J.B., M.P.W., and R.F.H. Project administration: R.F.H. Supervision: R.F.H. Writing—original draft: J.D.L. and R.F.H. Writing—review and editing: N.N., B.A.M., S.S.-H., R.T.K., J.B., M.P.W., and J.J.L. **Competing interests:** M.P.W. serves as a consultant for and has equity interest in Bryte, SleepFoundation, Oura, Restore Sleep, and StimScience. R.T.K. and J.J.L. are advisors to StimScience. All other authors declare that they have no competing interests. **Data and materials availability:** All data needed to evaluate the conclusions in the paper are present in the paper and/or the Supplementary Materials. Freely available software and algorithms used for analysis are listed where applicable.

Submitted 12 June 2023
Accepted 25 July 2023
Published 25 August 2023
10.1126/sciadv.adj1895